



Arab American University

Faculty of Graduate Studies

**Charge Carrier-Plasmon Interactions at the (In, Pb,
La)/CuSe Interfaces**

By

Arwa N. Abu-Ghannam

Supervisor

Prof. Dr. Atef Qasrawi

**This thesis was submitted in partial fulfillment of the
requirements for The Master's degree in Physics**

June/2019

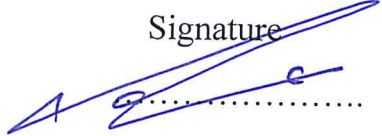

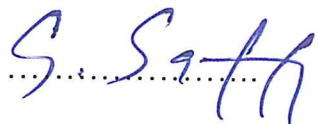
**© Arab American University-2019. All rights
reserved.**

**Charge Carrier-Plasmon Interactions at the (In, Pb, La)/CuSe
Interfaces**

By
Arwa N. Abu-Ghannam

This thesis was defended successfully on 26/6/2019 and approved by:

Committee members

	Signature
1. Prof. Dr. Atef Qasrawi (Supervisor)	
2. Assoc. Dr. Adli Saleh (Internal Examiner)	
3. Prof. Dr. Ghassan safarini (External Examiner)	

Declaration

The work in this thesis, unless otherwise referenced, is the researcher's own work and has not been submitted elsewhere for any other degree or qualification.

Student's name:

Signature:

Date:

Dedication

To My Family

Acknowledgments

Thanks to Allah Almighty who enable me to do this research. I also place on record, my sense of gratitude to one and all who, directly or indirectly, have lent their helping hands in this thesis.

First, it is a genuine pleasure to express my deep sense of thanks and gratitude to my mentor, philosopher and guide Prof. Dr. Atef Qasrawi, who created the small scientist inside me.

Endless thanks for my first teachers, my big family members. Also, I revere the patronage and moral support extended with love by my small family: Hani and Laya.

There are no bonds in expressing my gratitude to my friend Olfat Omarya; the research assistant in the physics research LAB. Her love, help and encouragement were a great support throughout the course of this work.

I am deeply indebted to my respected teachers of physics department in Arab American university: Prof. Dr. Zaki Saleh, Dr. Adli Saleh, Dr. Muayad Abu-Saa, Dr. Ahmad Omar, Prof. Mohammad Abu-Samra, Dr. Suliman Rabaa and Mr. Anan Hussien. I also would like to express a great thanks to Dr. Hazem Khanfar, the member of telecommunication engineering department, for his technical support.

Abstract

In this thesis, we have studied the structural and optical performances of CuSe thin films which are grown onto thin transparent Indium, Lanthanum and Lead metal substrates. The metal/CuSe films which are prepared by thermal evaporation technique under vacuum pressure of 10^{-5} mbar displayed different characteristics based on the metal type. Particularly, while the (In, Pb)/CuSe displayed the same value of cubic lattice constant, the La/CuSe exhibited shorter lattice constants. The structural parameters, accordingly are also influenced by the substrate type. Namely, the defect density, the stacking faults and the stress, exhibit higher values in the presence of La compared to of (In, Pb)/CuSe interfaces. The grain size decreases from 28 nm for glass/CuSe to 16 nm for La/CuSe while it increases to 36nm, 33nm in the presence of In and Pb substrates.

On the other hand, the optical spectroscopy studies which are carried out in the incident light wavelength range of 300-1100 nm revealed a smaller effect of the presence of metals on the value of the energy band gap and remarkable effect dielectric constant in the high frequency range. In addition, the Drude-Lorentz analysis and modeling on the imaginary part of the dielectric constant have shown that the scattering time at femtosecond level is increased in the presence of metal substrates from 1.50 to 2.50, 1.55 1.80 in the presence of glass, In, La and Pb substrates, respectively. Such behavior indicates that the electronic friction in CuSe has decreased and the electronic transport become more effective. Consistently, the

drift mobility is increased in the presence of metals. With the value of plasmon frequency are 3.38, 2.71, 1.66 and 2.38 being in the gigahertz range for glass, In, La and Pb substrates, respectively. The In, La, Pb/CuSe can be accepted as promising interfaces for use as plasmonic devices and as microwave filters.

List of contents

	Title	Page No.
	List of Tables	x
	List of Figures	xi
	List of Symbols	xiii
Chapter One	Introduction and Literature Survey	1
Chapter Two	Theoretical Background	
	2.1 X-ray diffraction (XRD)	5
	2.2 Dislocation Density	6
	2.3 Grain Size	7
	2.4 Micro-Strain and Stress	7
	2.5 Drude-lorentz model	8
Chapter Three	Experimental Approach	
	3.1 Substrate cleaning	12
	3.2 Thin film preparation	12
	3.3 The X-ray diffraction (XRD) measurements	14
	3.4 The hot-probe technique	15
	3.5 Optical measurements	16
	3.6 Software packages	17
Chapter Four	Results and Discussion	
	4.1 Structural Analysis	18

4.2	Optical Analysis	28
4.3	Effects of In, La and Pb on the dielectric properties of Cu ₂ Se	44
Chapter Five	Conclusions and Further Work	55
References		56
List of publications		62
Abstract in Arabic		63

List of Tables

No.	Title	Page No.
4.1.1	Mechanical properties of glass/CuSe, In/CuSe, La/CuSe and Pb/CuSe	24
4.3.1	Optical conductivity parameters for glass/Cu ₂ Se, In/Cu ₂ Se, La/Cu ₂ Se and Pb/Cu ₂ Se films.	54

List of Figures

No	Caption	Page No.
2.1.1	(a) X-rays scattering on crystal planes. (b) A diffraction peak at Bragg angle (Θ)	6
3.2.1	The 600 VCM evaporation system	12
3.2.2	The Inficon STM-200 thickness monitor	13
3.2.3	The images of (a) glass/Cu ₂ Se sample, (b) In/Cu ₂ Se sample, (c) La/Cu ₂ Se sample and (d) Pb/Cu ₂ Se	14
3.3.1	The Rikagu diffractometer	15
3.5.1	The thermos-scientific evolution 300 spectrophotometer	17
4.1.1	The X-ray diffraction spectrum of Copper Selenide grown onto glass	19
4.1.2	The X-ray diffraction spectrum of Indium, Copper Selenide and Copper Selenide on Indium	20
4.1.3	The X-ray diffraction spectrum of Lanthanum, Copper Selenide and Copper Selenide on Lanthanum	21
4.1.4	The X-ray diffraction spectrum of Lead, Copper Selenide deposited on glass and Copper Selenide deposited onto Lead	22
4.2.1	The optical transmittance of Indium, Copper Selenide on glass and Copper Selenide on Indium substrates	29
4.2.2	The optical transmittance for Lanthanum, Copper Selenide on glass and Copper Selenide on Lanthanum substrates.	30
4.2.3	The optical transmittance for Lead, Copper Selenide on glass and Copper Selenide on Lead substrates.	31
4.2.4	The optical reflectance for Indium, Copper Selenide on glass and Copper Selenide on Indium substrate.	32
4.2.5	The optical reflectance for Lanthanum, Copper Selenide on glass and Copper Selenide on Lanthanum substrates.	33

4.2.6	The optical reflectance for Lead, Copper Selenide on glass and Copper Selenide on Lead substrates.	34
4.2.7	The optical absorption coefficient for Copper Selenide on glass, Copper Selenide on Indium, Copper Selenide on Lanthanum and copper Selenide on Lead.	36
4.2.8	The $(\alpha E)^{1/p} - E$ variations for glass/Cu ₂ Se and In/Cu ₂ Se for (a) p=2, (b) p=1/3, (c) p=2/3 and (d) p=1/2	37
4.2.9	The $(\alpha E)^{1/p} - E$ variations for glass/Cu ₂ Se and La/Cu ₂ Se for (a) p=2, (b) p=1/3, (c) p=2/3 and (d) p=1/2	38
4.2.10	The $(\alpha E)^{1/p} - E$ variations for glass/Cu ₂ Se and Pb/Cu ₂ Se for (a) p=2, (b) p=1/3, (c) p=2/3 and (d) p=1/2	39
4.2.11	The $(\alpha E)^2$ versus E plotting for Cu ₂ Se and In/Cu ₂ Se.	40
4.2.12	The $(\alpha E)^2$ versus E plotting for Cu ₂ Se and La/Cu ₂ Se.	41
4.2.13	The $(\alpha E)^2$ versus E plotting for Cu ₂ Se and Pb/Cu ₂ Se.	41
4.3.1	The real part of the dielectric constant for glass/ Cu ₂ Se and In/Cu ₂ Se.	45
4.3.2	The real part of the dielectric constant for Cu ₂ Se/glass and La/Cu ₂ Se.	46
4.3.3	The real part of the dielectric constant for glass/Cu ₂ Se and Pb/Cu ₂ Se.	47
4.3.4	The imaginary part of the dielectric spectrum for Cu ₂ Se.	48
4.3.5	The imaginary part of the dielectric spectrum for In/Cu ₂ Se	49
4.3.6	The imaginary part of the dielectric spectrum for La/Cu ₂ Se.	50
4.3.7	The imaginary part of the dielectric spectrum for Pb/Cu ₂ Se.	51

List of Symbols

Symbol	Acronym
ε	The micro-strain
β	Peak broadening
Θ	Bragg angle
D	Grain size
d	Inter-planner distance
ν	Young's modulus
γ	The inverse of the electron scattering time
λ	Wavelength
δ	Dislocation density
SF%	Staking faults
t	Thickness
α	Absorbance
P	A constant related to the optical transition type
E_g	Energy gap
k	Extinction coefficient
ε_{eff}	The effective dielectric constant
ε_{im}	The imaginary part of the dielectric constant
ε_r	The real part of the dielectric constant
m^*	The effective mass
μ	The drift mobility
Δ_a	The lattice mismatch
w_s	The reduced resonance frequency
w_{ps}	The electron bounded plasma frequency

Chapter one

Introduction and literature survey

Plasmonics are promising and growing fields of science over the past decades. Nowadays, research interest has been extremely focused on Plasmon devices. This interest has arisen from its wide range of electronic and photoelectronic applications. Advanced plasmonic interfaces are used in photovoltaics in order to optimize the light trapping [1]. As for examples, ultrasensitive detection of molecules is obtained by surface Plasmon resonance sensors with graphene-MoS₂ hybrid structures [2]. As particular application, exciton-plasmon coupling interactions finds applications in solar cells, quantum information processing, light emitting diodes, low threshold lasers and biomedical detection [3]. Plasmon waveguides in a graphene-based nanostructure are novel in the fabrication of sensors and logic gates [4]. Tunable Plasmon-induced transparency effect in the mid -IR range is used to fabricate plasmonic refractive indices sensors and multi-channel-selective filters [5]. Gold nano cup has interested application in planner plasmon devices [6]. InSe/CdSe bilayer plasmon cavity is reported as promising cavities for high- performance optoelectronic devices being operative at very high frequencies [7].

Many researchers focused on metal-semiconductor contacts in order to study plasmon-electron interactions. Studies on Yb/InSe interface electronic properties and optical conductivity spectra indicated that the interfaces are promising in the manufacturing of thin film transistors [8]. In/ β -Bi₂O₃ and Yb/ γ -Bi₂O₃ interfaces acted like microwave traps with a relatively high microwave absorbability at the frequency of 1200 MHz, so it is applicable as microwave resonator and as fast

electronic switching device [9]. In addition, CMOS digital logic devices which are synthesized using a Yb/Bi₂O₃/Au interface reveal a 10^5 rectification ratio [9]. Drude-Lorentz model analysis on Ge/Ga₂S₃ interface has resulted in Plasmon frequency in the range of 1.33-2.30 GHz [10]. Due to this feature, it is novel for use in wireless technology as terahertz receivers and as microwave cavity [10]. In addition, Au nanosandwiching of InSe thin films which has a plasmon frequency of 1.53 GHz is used in the engineering of photovoltaic materials [11]. Moreover, electrons bounded plasmon frequencies and a resonant frequency of Y/InSe interface is suggested for possible application in terahertz technology [12]. Wide tunable plasmonic surface frequency which is achieved via thickness control of Mg layers on the Bi₂O₃ semiconductor is reported to be suitable as plasmonic surface stabilizers and as microcavities [13].

One material which is proposed for plasmonic interfaces is Copper Selenide (CuSe). CuSe is one of the I-VI semiconductors that is subjected to extensive research, because of its unique optical absorption and electrical conduction [14]. Its optical band gaps are determined at 298 K by optical absorbance and diffuse reflection spectra to be 2.5 eV and 1.84 eV for direct and indirect transitions, respectively [15, 16]. However, on the electrical side, CuSe has a resistivity value of $2.12 \times 10^{-3} \Omega \cdot \text{cm}$ at 200 °C [17]. It exhibits p-type conductivity as discovered by Hall effect measurements [18]. X-ray diffraction analysis showed that CuSe has hexagonal structure [16]. Deposition of CuSe films at different substrate temperatures showed transformation from orthorhombic to cubic structure [19]. Also, it displays a

significant effect on its optical and electrical properties, strong absorption in the blue region and electrical resistivity in the order of $10^{-4} \Omega \cdot \text{cm}$ [19].

Due to these properties, it finds applications in many optoelectronics. As an example, CuSe nanosheets are used in photoelectric devices as a potential material for optoelectronics [16]. Furthermore, CuSe thin film electrodes yield a relatively high photo-electrochemical conversion efficiency of about 14.6 % [20]. Also, it plays a significant role in increasing the power efficiency of quantum dots sensitized solar cells from 0.69 % to 1.68 % in the presence of Platinum and CuSe counter electrode respectively [21]. Moreover, solid-state supercapacitor, which is fabricated using CuSe at Co(OH)_2 nanosheets displayed capacitance values of 441.4 mF cm^{-3} [22].

Various methods have been used for the synthesis of CuSe. For example, simple and rapid hydrothermal process for production of homogenous and highly crystalline nanoplates [16], electrochemical followed by chemical bath deposition for thin films production [20], spin coating and co-reduction methods are famously employed techniques to prepare thin films [17].

On the other hand, different doping profiles lead to a noticeable change in the structural, optical and electrical properties of CuSe. For example, Na^+ ion-doped Cu_2Se reflects less electrical conductivity than un-doped one, higher absorption in the visible light range which correspond to a band gap energy range between 2.5-1.52 eV and exhibited a p-type conductivity [23]. However, 4% S-doped Cu_3Se_2 enhances the photocatalytic performance under solar light irradiation, increasing the sulfur concentration to 6% caused an increase in the band gap value [24]. n-type

conductivity appears in the case of Bi^{+3} dopant and strong band gap emission at 629 nm, with a band gap increase as a result of increasing the dopant content [25]. Furthermore, a polycrystalline nature appears in presence of Al^{+3} . It is associated with a decrease in the resistivity and direct band gap [26]. In another work, Li-doped films displayed similar thermal conductivity as CuSe, but with higher effective mobility [27].

The above-mentioned information motivated us to explore the effects of metal substrates on the performance of CuSe. We aim to discuss the structural, optical and electrical properties of these films. Energy band gap attenuations and plasmonic interactions will be studied for Copper Selenide films which are prepared onto transparent In, La and Pb substrates as plasmonic interfaces. As though in the second chapter we will report some of the important theoretical notes that are needed to analyze the measurements. In the third chapter we focus on some of the experiments and their procedures. Finally, we will introduce our results and discuss them extensively in chapter Four.

Chapter Two

Theoretical Background

2.1 X-ray diffraction (XRD)

X-rays are electromagnetic radiation with wavelength ranges from 0.1 to 100 Å. The wavelength of X-rays used in XRD is about 1 Å, which is comparable to the value of crystal's interatomic spacing. When X-ray beams with certain wavelengths hits a sample, X-rays with the same wavelength are scattered. The spatial distribution and intensities of the scattered X-rays form diffraction patterns. These patterns determine the structure of the sample. Generally, samples can have ordered structure such as single crystals or disordered like glasses [28]. For an elastic scattering, the incident and reflected rays make equal angles with the crystal planes ($\Theta_i = \Theta_r = \Theta$) as shown in figure 2.1.1 (a), the peak is observed if Bragg's law is satisfied:

$$2 d \sin\theta = n \lambda \quad 2.1.1$$

Where d is the distance between each adjacent plane, Θ is the Bragg angle at which the X-rays are incident, n is an integer and λ is the wavelength of the X-rays [29]. Schematic plot of the resulting peak is displayed in figure 2.1.1(b).

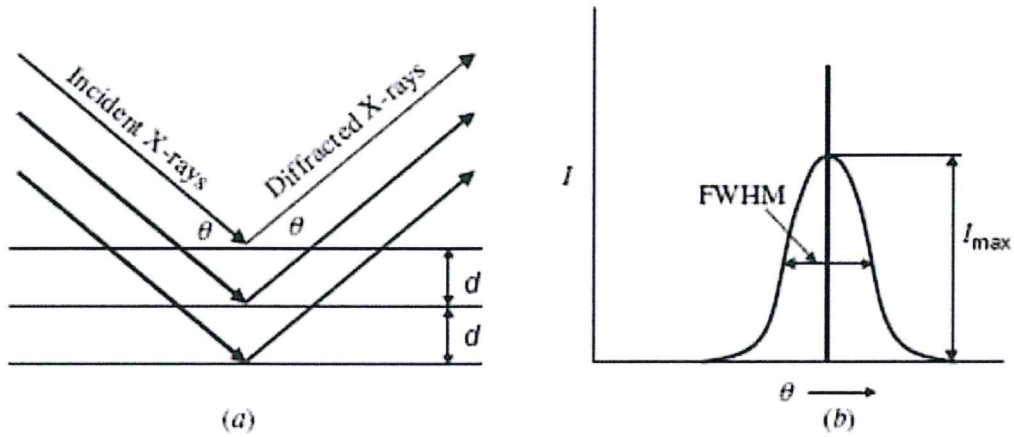


Figure 2.1.1 (a) X-rays scattering on crystal planes. (b) A diffraction peak at Bragg angle (Θ).

2.2 Dislocation Density

Although crystals have high order of atomic arrangements depending on its structure, most crystalline materials are never perfect. Crystal defect can interrupt the atomic arrangement leading to an interprets in the material macroscopic properties like its strength and failure. There are different types of defects, such as point, line, planner and bulk defects. Dislocations are line defects with two types, the screw and edge dislocations [28].

Dislocation density is the length of the dislocation lines per unit area. The following relation is used to calculate the dislocation density (δ) in (line /cm²) [30]:

$$\delta = \frac{15 \varepsilon}{a D} \quad 2.2.1$$

Where ε is the micro-strain, a is the lattice constant and D is the crystallite size.

2.3 Grain Size

A broadening in the diffracted X-ray line will occur for crystallite size less than approximately 1000 Å. The presence of broadening is described by β , which is the full width at half maximum (FWHM). The FWHM is shown in figure 4.1.1 (b). This broadening is used to estimate the grain or crystallite sizes (D) using the Scherrer's relation [31]:

$$D = \frac{K \lambda}{\beta \cos \theta} \quad 2.3.1$$

Where k is a dimensionless constant related to the crystallite shape and has a typical value of about 0.94, but varies with the actual shape of the crystallite. In addition, λ is the wavelength, β is the FWHM in radian and θ is the diffraction angle. Scherrer's equation is valid only for crystallites of size less than 200 nm.

2.4 Micro-strain and Stress

The micro-strain (ε) can be determined from the XRD peak broadening according to:

$$\varepsilon = \frac{\beta}{4 \tan \theta} \quad 2.4.1$$

The crystal strain is related to the crystal defects. It increases because of the generation of dislocations [30].

Another parameter can be obtained from the strain is the stress. Stress and strain are related to each other by the young's modulus as follows:

$$S = \gamma \varepsilon \quad 2.4.2$$

Where S is the stress and γ is the young's modulus [30].

2.5 Drude-lorentz Model

Drude model is a simple classical model for conductivity, in which the optical constants are related to the electronic properties of solids through the free carriers. This model starts with the equation of motion of an electron in the presence of a periodic optical electric field, which states that:

$$m \frac{dV}{dt} + \frac{mV}{\tau} = eE_0 e^{-i\omega t} \quad 2.5.1$$

Where v is the drift velocity for the carrier and τ is the relaxation time and $E_0 e^{-i\omega t}$ is the sinusoidal electric field. As a response to this field, electrons move in a sinusoidal manner. The motion of the electrons can be described by:

$$v = v_0 e^{-i\omega t} \quad 2.5.2$$

The substituting of equation 2.5.2 in 2.5.1 gives:

$$\left(-mi\omega + \frac{m}{\tau}\right) v_0 = eE_0 \quad 2.5.3$$

However, the amplitude of the velocity (v_0) and the field (E_0) are related through the current density (j) by:

$$\mathbf{j} = ne\mathbf{v}_\circ = \sigma \mathbf{E}_\circ \quad 2.5.4$$

Where \mathbf{j} is the current density and σ is the conductivity. Substitution for (\mathbf{v}_\circ) yields:

$$\mathbf{v}_\circ = \frac{e \mathbf{E}_\circ}{(m/\tau) - i\omega m} \quad 2.5.5$$

Finally, the complex conductivity are:

$$\sigma = \frac{n e^2 \tau}{m(1 - i\omega\tau)} \quad 2.5.6$$

When an electric field is applied in one direction it can produce force in the other directions due to the isotropy of the constant energy surfaces in solids. The current density and the electric field are related through the tensorial relation:

$$j_\alpha = \sigma_{\alpha\beta} E_\beta \quad 2.5.7$$

Here $\sigma_{\alpha\beta}$ is a second rank tensor, that can have off-diagonal terms. These terms are due to the effective mass tensor, the following relation describe the effective mass tensor in terms of the curvature of the energy band $E(\mathbf{k})$

$$\left(\frac{1}{m}\right)_{\alpha\beta} = \frac{1}{\hbar^2} \frac{\partial^2 E(\mathbf{k})}{\partial k_\alpha \partial k_\beta} \quad 2.5.8$$

For semiconductors with narrow band gaps, $m_{\alpha\beta}$ is function of the energy. In addition, the validity of Drude formula is restricted to two conditions. The effective mass tensor is evaluated at the Fermi level and take into account the total electron density. Then, the total complex dielectric function with the consideration of the core dielectric constant (ϵ_{core}) is:

$$\varepsilon(w) = \varepsilon_{core}(w) + 4\pi i \sigma / w \quad 2.5.9$$

So that:

$$\sigma(w) = (ne^2 \tau / m^*) (1 - iw\tau)^{-1} \quad 2.5.10$$

In which $(4\pi \sigma / w)$ is the imaginary part of the free carrier contribution. From the Drude theory:

$$\varepsilon = \varepsilon_{core} + \frac{4\pi i}{w} \frac{ne\tau^2}{m(1-iw\tau)} = (\varepsilon_1 + i\varepsilon_2) = (n_1 + ik_2)^2 \quad 2.5.11$$

Where ε_1 and ε_2 is the real and imaginary parts of the dielectric constant, respectively [32].

The Drude model needed to be modified and adapted by adding the Lorentz model to be used for semiconductors if the free carrier density introduced through doping is sufficiently high to cause the semiconductor behaves similarly to the metal [33-34].

The dielectric function described by the Drude-Lorentz model can used to obtain the dispersion relation [35]:

$$\varepsilon(w) = 1 - \sum_i^N \frac{w_{pi}^2}{(w^2 + iw\gamma_i)} + \sum_i^N \frac{w_{pi}^2}{(w_i^2 - w^2) + iw\gamma_i} \quad 2.5.12$$

Where i refer to the relative peak. $w_p = \sqrt{4\pi ne^2 / m^*}$ is the electron bounded plasma frequency. n and m^* are the free electron density and the effective mass of free electrons, respectively. w being the reduced resonant frequency, and γ is the damping rate.

This model enables taking advantage of semiconductors at optical frequencies and searching for a possibility of an optical plasmon existence in that range.

Chapter Three

Experimental Approach

In this chapter, we report and discuss some of the methods that we use to produce the plasmonic interfaces. Particularly, the methods of preparing the thin films are described in detail.

3.1 Substrate cleaning

Many substrates are used to prepare films, such as glass and ceramics. The substrate used in preparing our samples was Pyrex microscopic glass slides, which were cleaned using alcohol to remove dust from the surface. Then, they were treated ultrasonically at 60°C for 20 minutes. The cleanness of the surface was tested by optical methods and continuous liquid film flowing.

3.2 Thin film preparation

Copper Selenide thin films were prepared by the thermal vapor deposition technique under vacuum pressure of 10^{-5} mbar using VCM-600 evaporator. The evaporation system, which is shown in figure 3.2.1, consists of a vent valve to enter and exit air to the system, shutter controller to control the amount of vapor in the system, current controller to control the amount current (maximum current of 150 A), cooling system, and vacuum pump. A Tungsten boat is used to heat the evaporation sources for each film.



Figure 3.2.1 The 600 VCM evaporation system.

Indium, Lanthanum, Lead and Copper Selenide powder were placed in their own tungsten boats during their own evaporation cycles. Each boat was fixed in the evaporation system. A metal plate was used to hold the glass substrates. Also, a crystal oscillator thickness monitor was used to measure the thickness of the films during evaporation. The thickness monitor which is shown in figure 3.2.2 was Inficon STM-2 types that can evaluate 3000 measurements per second and have resolution of 0.03 Å. The In, La and Pb films thicknesses were 150 nm and Copper Selenide film was of 1.0 µm thickness. A layer of Copper Selenide (1.0 µm) was deposited on In, La and Pb films, the images of the samples are shown in figure 3.2.3. As seen from the figure, while the film color of the Cu₂Se grown onto glass is brown (figure 3.2.3(a)), Indium caused dark brown colored films (3.2.3(b)), Lanthanum make the film sandy brown (3.2.3(c)) and Lead make the color olive (3.2.3(d)).

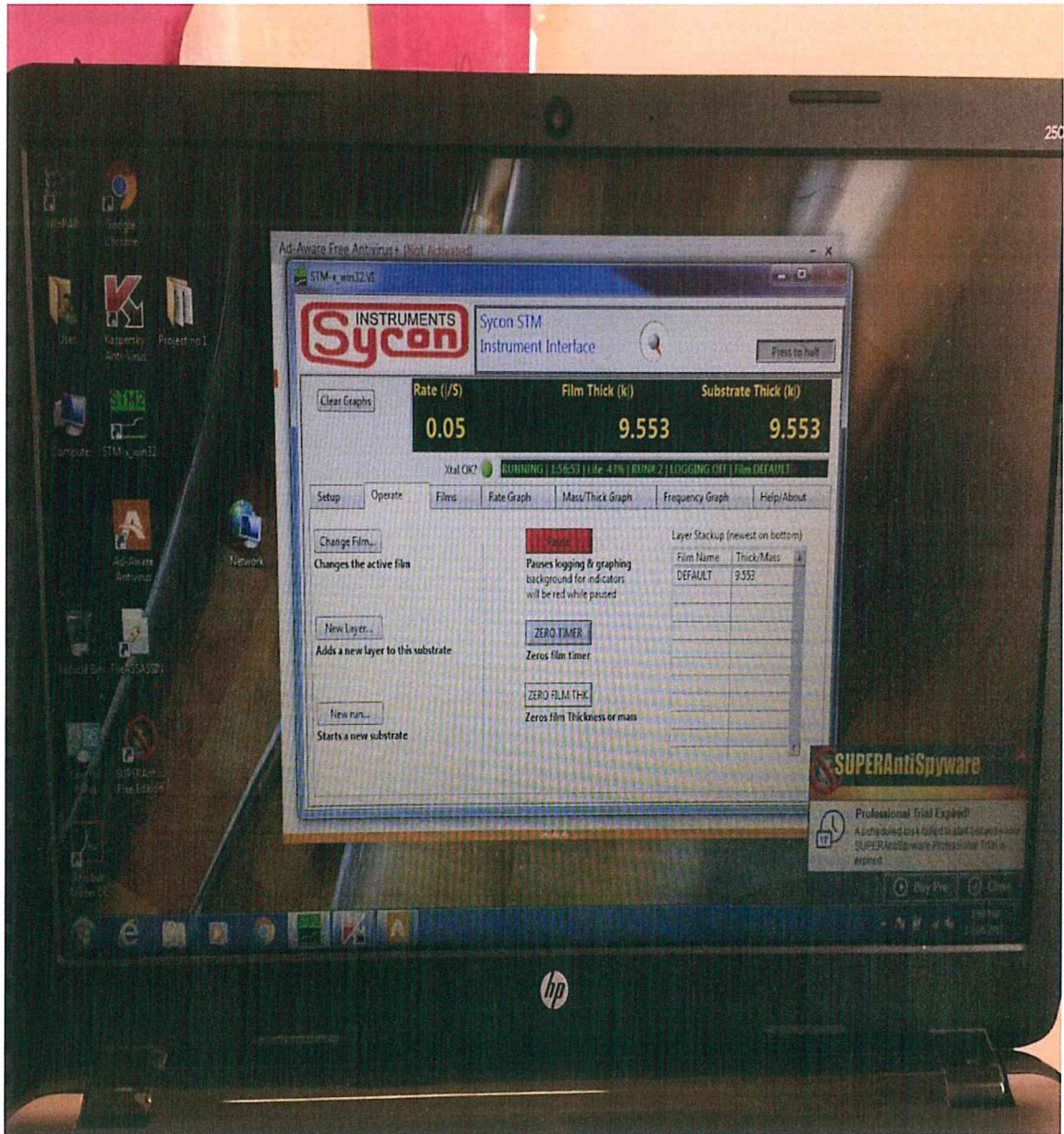


Figure 3.2.2 The Inficon STM-2 thickness monitor.

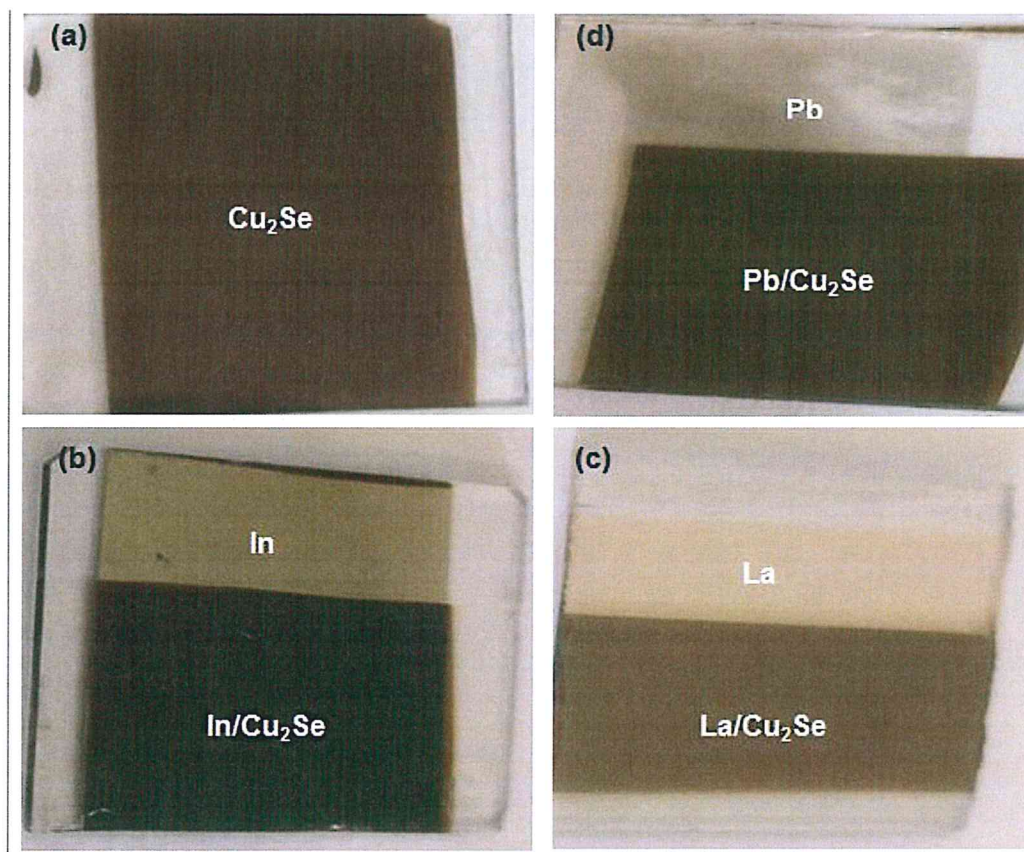


Figure 3.2.3 The images of (a) glass/ Cu_2Se sample, (b) In/ Cu_2Se sample, (c) La/ Cu_2Se sample and (d) Pb/ Cu_2Se

3.3 The X-ray diffraction (XRD) measurements

The Rikagu diffractometer equipped with K_α radiation of Copper anode of 1.4505 \AA wavelength was used to explore the structure of the samples. The exciting voltage was 40 KV to produce electrons beam of 15 mA. So that the power of X-ray is 600 Watt. The X-ray unit is used to determine the crystal structure of glass/Copper Selenide, In/Copper Selenide, La/Copper Selenide and Pb/Copper Selenide interfaces. The XRD

system shown in figure 3.3.1 consists of X-ray source (generate characteristics X-ray), sample holders (a clay is used to fix the sample on it) and detector (detect the intensity of the reflected beam). The scanning speed was $1^\circ/\text{min}$ with a step of 0.05. Moreover, the diffraction angle (2θ) was varied from 10° to 70° .



Figure 3.3.1 The Rikagu diffractometer.

3.4 The hot-probe technique

The hot-probe technique is used to determine the conductivity type of the Copper Selenide semiconductor using a heater and a digital multi-meter (DMM). The hot and

cold parts were connected to the positive and negative terminals of the DMM respectively. As a result, the carriers (electrons in n-type and holes in p-type) move from the hot part to the cold one. Therefore, a negative reading on the DMM indicate a p-type while a positive one indicate a n-type. A negative voltage was read on the DMM when the probes were applied to the Copper Selenide film, indicating the p-type semiconductor.

3.5 Optical measurements

A thermo-scientific evolution 300 spectrophotometer which is equipped with VeeMax II spectrophotometer was used to measure the optical transmittance and reflectance in the range of 300-1100 nm incident light wavelengths. The system includes silicon photodiode detectors with extended wavelength ranges from the Ultraviolet to near Infrared. In addition, a VISION software was used to collect and manipulate data as shown in figure 3.5.1.

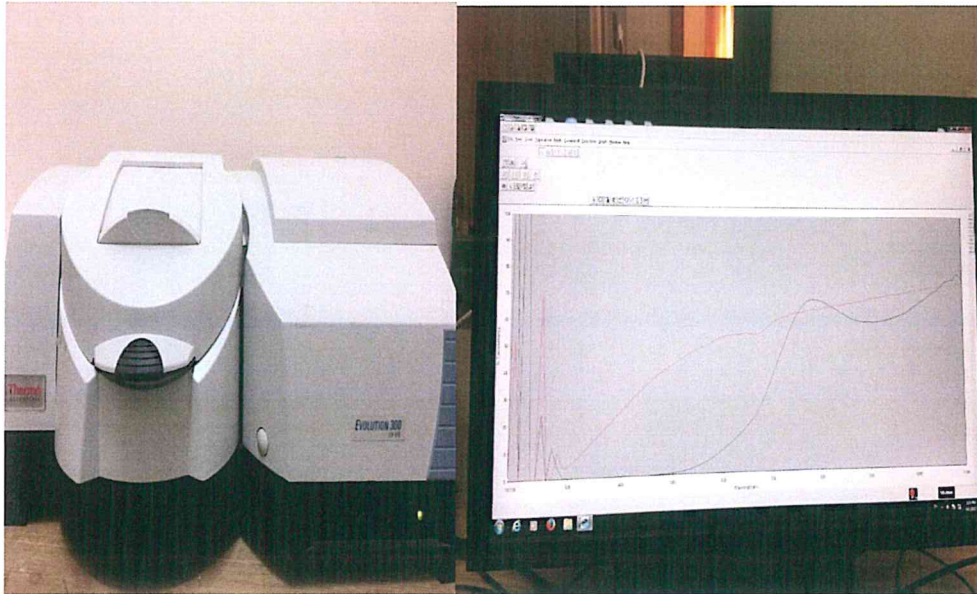


Figure 3.5.1 The thermoscientific evolution 300 spectrophotometer.

3.6 software packages

TREOR 92 was used to analyze the X-ray diffraction patterns, to determine the crystal structure of glass/Copper Selenide, Indium/Copper Selenide, Lanthanum/Copper Selenide and Lead/Copper Selenide. The software provides two choices for solution. One request the observed diffraction angle values and determine both of the lattice constants and Miller indices based on suggested crystal structure. The other, request crystal structure and lattice constants to produce the observed diffraction angles and Miller indices.

Chapter Four

Results and Discussion

4.1 Structural Analysis

Copper Selenide thin films are deposited onto glass, indium, lanthanum and lead substrates. In order to study the effects of lattice mismatches due to different substrate structures on the mechanical properties of Copper Selenide films, the X-ray technique is used.

XRD for Copper Selenide deposited onto glass is presented in Fig 4.1.1. As shown from the figure, Copper Selenide exhibits crystalline nature pronounced by four reflection peaks. The peaks are at diffraction angles (2θ) of 24.45° , 27.1° , 31.1° , 44.58° corresponding to intensity values of 3555, 10924, 4567, 1158. In order to determine the structures that are correlated to these peaks, literature data were used. Based on literature [36-37], copper selenide has more than one probable structure: cubic, hexagonal, orthorhombic and tetragonal structure phase. Data analysis for each structure depending on the lattice parameters was carried out by TREOR 92 software. Comparison between the obtained and observed values for the last three peaks revealed that the most closed structure is the cubic one. All the observed peaks are indexed in accordance with the cubic phase except for the peak centered at 24.45° . This peak exhibit relative intensities of 24.6% and mostly related to orthorhombic CuSe and assigned to the (014) plane orientation. The Miller indices for each peak are shown in figure 4.1.1.

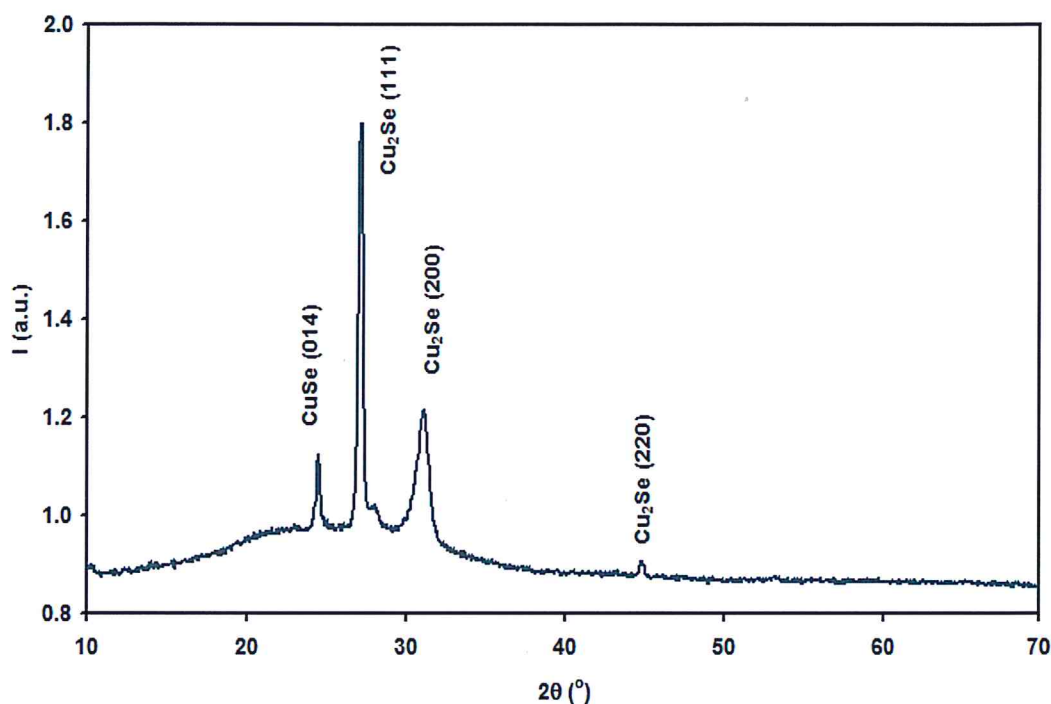


Fig. 4.1.1 The X-ray diffraction spectrum of Copper Selenide grown onto glass

In the presence of In substrate, the number of peaks is increased to six peaks. Namely, they are centered at 2θ values of 24.55° , 27.20° , 29.95° , 31.15° , 33.20° and 44.85° corresponding to intensity values of 2570, 6780, 2194, 2097, 4506 and 1186, respectively. As indexed in figure 4.1.2, some peaks are related to Indium metal and others are related to Copper Selenide phases. The minor orthorhombic peak of CuSe appeared again side by side with the three cubic Cu₂Se peaks. The relative intensity of the minor peak is increased to 27.4 %. In other words, Indium maintains the ratio of cubic to orthorhombic phases as in Copper Selenide/glass which was nearly 70%. For deep analysis, zoom of the intensive peak is displayed in figure 4.1.2. As one can see, the peak in the presence of Indium is shifted to the right with higher value of 2θ . At the same time, Indium metal decreased the intensity of the main peak.

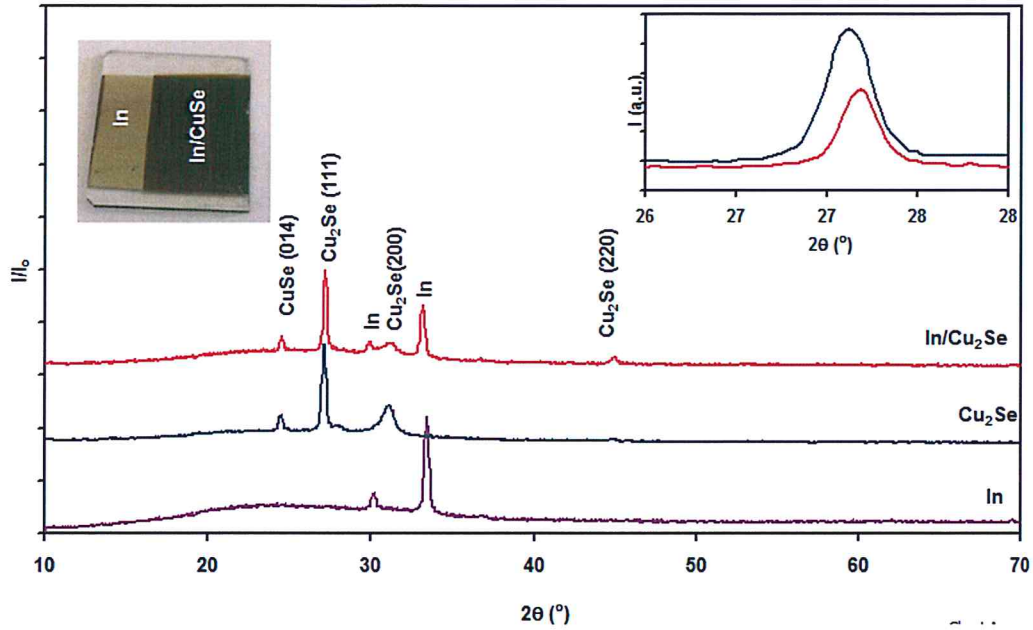


Fig. 4.1.2 The X-ray diffraction spectrum of Indium, Copper Selenide on glass and Copper selenide on Indium.

When Copper Selenide was deposited onto amorphous Lanthanum films, as shown in figure 4.1.3, the number of peaks also increased to six peaks. The 2θ values are 24.65° , 27.3° , 31.25° , 42.65° , 45.05° and 49.8° corresponding to intensity values of 2556, 7398, 3119, 1816, 1350, 1232, respectively. Again the three peaks of cubic Cu_2Se peaks appeared as well as one peak which is assigned to the minor phase. According to the literature data, the rest of the peaks are related to Lanthanum metal. It decreases the intensity of the (111) peak leading to an increase in the relative intensity of the (014) peak to 24.7%. A deep look at the peak of maximum reflection shows that Lanthanum substrate caused a shift to the right by 0.20° .

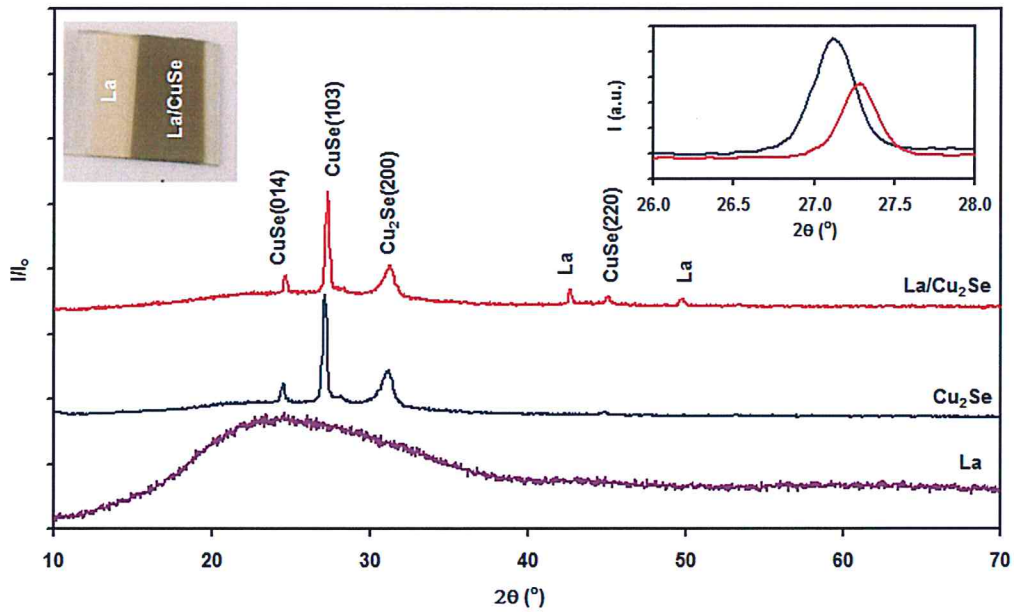


Fig. 4.1.3 The X-ray diffraction spectrum of Lanthanum, Copper Selenide on glass and Copper selenide on Lanthanum.

All the previous peaks of copper Selenide phases have appeared again in the case of amorphous Lead substrate as shown in figure 4.1.3, but with a slight different diffraction angles from values of the angles of Copper Selenide deposited onto glass. The peaks are at 24.60° , 27.20° , 28.20° , 31.25° , 44.90° , with relative intensity of 2528, 6735, 1811, 2693, 1072. The new peak (28.20°) is related to Lead metal [for the XRD patterns that we measured in our lab]. The presence of Pb substrate changes the intensity of the peaks. In other words, it shifts the maximum peak toward a higher angle and smaller intensity. The minor orthorhombic peak appears with 27.3% relative intensity.

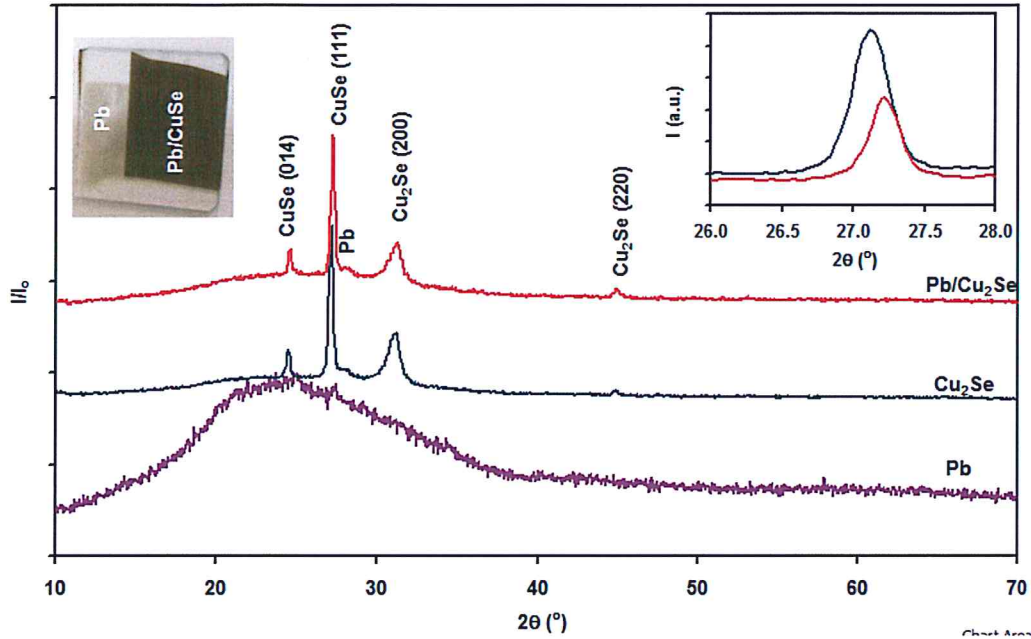


Fig. 4.1.4 The X-ray diffraction spectrum of Lead, Copper Selenide deposited onto glass and Copper selenide deposited onto Lead.

For detailed information about the substrate effect on Copper Selenide, in each case the lattice constant was calculated. The cell parameter of the cubic Cu_2Se is calculated to be $a=5.697 \text{ \AA}$, which matches the literature value being $a=5.719 \text{ \AA}$ [28]. While as the above results show, in the presence of all metals the maximum peak is shifted toward a larger angles. So according to Bragg's law, one expects that the interatomic distance will decrease as also the lattice constant does. Calculation for the lattice parameters of Cubic Cu_2Se on (glass, In, La and Pb) verified this explanation. The obtained values are illustrated in table 4.1.1. As the table shows, the lattice constants are 5.676 \AA , 5.656 \AA and 5.676 \AA for Cu_2Se grown onto Indium, Lanthanum and Lead substrates, respectively. All these values are different from that of Copper Selenide on glass, Indium is differing by 2.1%, Lanthanum by 4.1% and Lead by 2.1%.

After we find the new lattice constants for Copper Selenide in the presence of all substrates, it is interesting to calculate the lattice mismatch between each metal and the cubic Copper Selenide using the following equation:

$$\Delta_a = \frac{|a_{\text{substrate}} - a_{\text{epitaxial}}|}{a_{\text{epitaxial}}} \times 100\% \quad (4.1.4)$$

Indium substrate has tetragonal structure with ($a = 3.2523\text{\AA}$ and $c = 4.9555\text{\AA}$), Lanthanum metal has hexagonal structure with ($a = 3.772\text{\AA}$ and $c = 12.141\text{\AA}$) while Lead has cubic structure with ($a = 4.9506\text{\AA}$). The obtained values for the lattice mismatch are reported in Table 4.1.1. The lattice mismatches in In/Cu₂Se interfaces are 42.7%, 12.7% along the a-axis and c-axis, respectively. However, the lattice mismatches in La/Cu₂Se are 33.3% and 114.6% along the a-axis and c-axis, respectively. While, the lattice mismatches in Pb/Cu₂Se are 12.8%.

The XRD patterns are also employed to study the mechanical parameters of the cubic Cu₂Se including grain size (D), strain (ϵ), stacking faults (SF%), dislocation density (δ) and stress (S). The grain size was calculated by means of Scherrer's equation,

$$D = \frac{0.94 \lambda}{\beta \cos \theta} \quad (4.1.1)$$

Where λ is the X-ray wavelength, β is the full width half maximum, and θ is diffraction angle of the observed peak.

In addition, the micro-strain (ϵ) was calculated according to the following relation:

$$\epsilon = \text{strain} = \frac{\beta \cos \theta}{4 \sin \theta} \quad (4.1.2)$$

Moreover, the dislocation density (δ) was calculated using the following:

$$\delta = \frac{15 \epsilon}{a D} \quad (4.1.3)$$

Where a is the lattice constant, D is the grain size.

In addition, stress (S) was obtained by the following relation:

$$S = \gamma \epsilon \quad (4.1.5)$$

Where γ is the young modulus of Copper Selenide ($\gamma=62\text{GPa}$) [38].

The calculated values are reported in Table 4.1.1.

Table 4.1.1 Mechanical properties of glass/CuSe, In/CuSe, La/CuSe and Pb/CuSe

	a (Å)	D (nm)	ϵ ($\times 10^{-3}$)	S ($\times 10^9$ dyne/cm ²)	SF%	δ ($\times 10^{11}$ line/cm ²)	Δa (%)	Δ_a	Δ_c
glass/CuSe	5.697	28	5.432	3.368	0.270	5.02	2.2		
In/CuSe	5.676	36	4.238	2.627	0.211	3.08	4.3	42.7	12.7
La/CuSe	5.656	16	9.882	6.127	0.493	16.87	6.3	33.3	114.6
Pb/CuSe	5.676	33	4.689	2.907	0.216	3.77	4.3	12.8	12.8

The decrease in the lattice parameters indicates that the presence of metals caused a deformation of the cubic cells of Cu₂Se. The presence of In, La and Pb atoms creates new forces, attraction forces with Se atoms and repulsive forces with Cu atoms leading to the calculated stress values which are shown in Table 4.1.1

The displacement of atoms affects the position of the cubic unit cell and also the lattice constant. So that, it is remarkable to look on the micro-strain values that is presented in Table 4.1.1. The micro-strain decreases when the material is coated onto In and Pb substrates. It decreases from 5.432×10^{-3} for Cu₂Se on glass to 4.238×10^{-3} and 4.689×10^{-3} , respectively. While it increases to 9.888×10^{-3} in the presence of La substrate.

The values in table 4.1.1 show that the grain sizes in the presence of Indium metal increased from 28 nm for glass/Cu₂Se to 36 nm. On the contrary, Lanthanum decreased the size of the grain to 13 nm. Lead also increase the grain size as Indium. The grain size in Pb/Cu₂Se is 33 nm.

An opposite trend of variations is observed in the dislocation density. As appeared from table 4.1.1, defects in Cu₂Se on glass are 5.02×10^{11} line/ cm². However, calculations show that the presence of Indium and Lead caused a decrease in the dislocation density. In contrast, Lanthanum increases the value of δ .

In order to understand the reason for this difference in metal's behavior on the defects, one may think about the dangling bonds on the surfaces of metals layers and copper selenide layer. The existence of incomplete bonds on the surface may lead to interaction between the metal and Selenium atoms to satisfy their bonds, so In₂Se₃, La₂Se₃ and PbSe₂ may have formed. But, this interfacial bond are still of less effect because no XRD peaks related to one of these were detected.

Another possible explanation is the atomic substitution. The existence of Copper vacancy in Cu₂Se gives metal atoms an opportunity to make atomic substitution [39].

This reasoning is acceptable for Indium and Lead because of their small ionic radii comparing to the Cu^{+1} radius, the ionic radii for In^{+3} , Pb^{+4} and Cu^{+1} are 0.92 Å, 0.94 Å and 0.98 Å, respectively [40-42]. Therefore, the defect density was decreased in copper selenide. On the other hand, Lanthanum atomic substitution is not possible because La^{+3} has ionic radii of 1.16 Å [43] so Lanthanum cannot substitute copper vacancy. Instead, it can make atomic interstitial substitutions, thus the defect density is increased.

On the other hand, the stacking faults percentage for glass/ Cu_2Se is 0.270%. Indium and Lead substrates decrease the percent to 0.211% and 0.216%, respectively. Alternatively, the presence of lanthanum substrate increases the faults percent to 0.493%. The trend of increase and decrease in the stacking faults is associated with the trend of the defect density. In addition, the interstitial substitution without reducing the Cu vacancy leads to defect crowding which is a probable reason for the increase in the strain in the case of Lanthanum.

One may also think about the repulsive bonds in each of the In/ Cu_2Se , La/ Cu_2Se and Pb/ Cu_2Se . Copper Selenide has two repulsive bonds: Cu-Cu, Se-Se and one attractive Cu – Se. The bond lengths of Cu-Cu, Se-Se and Cu-Se are 2.30 Å [44], 2.32 Å [45] and 2.39 Å [46], respectively. The presence of metal substrate adds repulsive bonds between Indium and cation atoms. For Indium substrate, the new bonds are: In-Se and In-In that have bond lengths of 2.69 Å [47] and 3.25 Å [45] respectively. According to the lengths, Indium atoms prefer the shortest bond, in other words it prefer Selenium rather than Indium atoms. Further, lanthanum bonds were calculated using crystal maker software packages and found to be 2.96 Å and 3.127 Å for La-La and La-Se one

by one. Thus La-Se is the preferable bond for La atoms. The same behavior is expected for Lead because Pb-Se bonds length which equals 3.05\AA [48] is shorter than Pb-Pb bond (3.50\AA) [49]. Other work revealed that Copper Selenide doped with Lead has tetragonal structure with lattice constants of $a=b=6.337\text{\AA}$ and $c=4.385\text{\AA}$ [50].

4.2 Optical Analysis

The spectral transmittance (T%) and reflectance (R%) for glass/Cu₂Se, In/Cu₂Se, La/Cu₂Se and Pb/Cu₂Se were recorded in the spectral range of 300–1100 nm using ultra-violet visible spectrophotometer. The optical transmittance spectra for glass/In(150 nm), glass/Cu₂Se and In/Cu₂Se samples are displayed in figure 4.2.1. As shown from the figure, the T% for In sample increases with increasing the incident light wave length. At 1100 nm the transmittance for In reaches 52%. While the T% for glass/Cu₂Se slowly varies then it undergoes a sharp increase exhibiting maximum values of 32.2% at 686 nm after that it decreases to reach low T% of 7.7% at 1100 nm. During the increase and decrease curves, the transmittance for Cu₂Se crosses that for In two times at 578 and 738 nm corresponding to T% of 18.9% and 31.9%, respectively. In addition, the T% for In/Cu₂Se is almost zero until λ exceeds 482 nm. It increases to a maxima of 6.7% at 826 nm then decreases and reaching 1.7%. In general, the presence of Indium decreases the transmittance for Cu₂Se to low values.

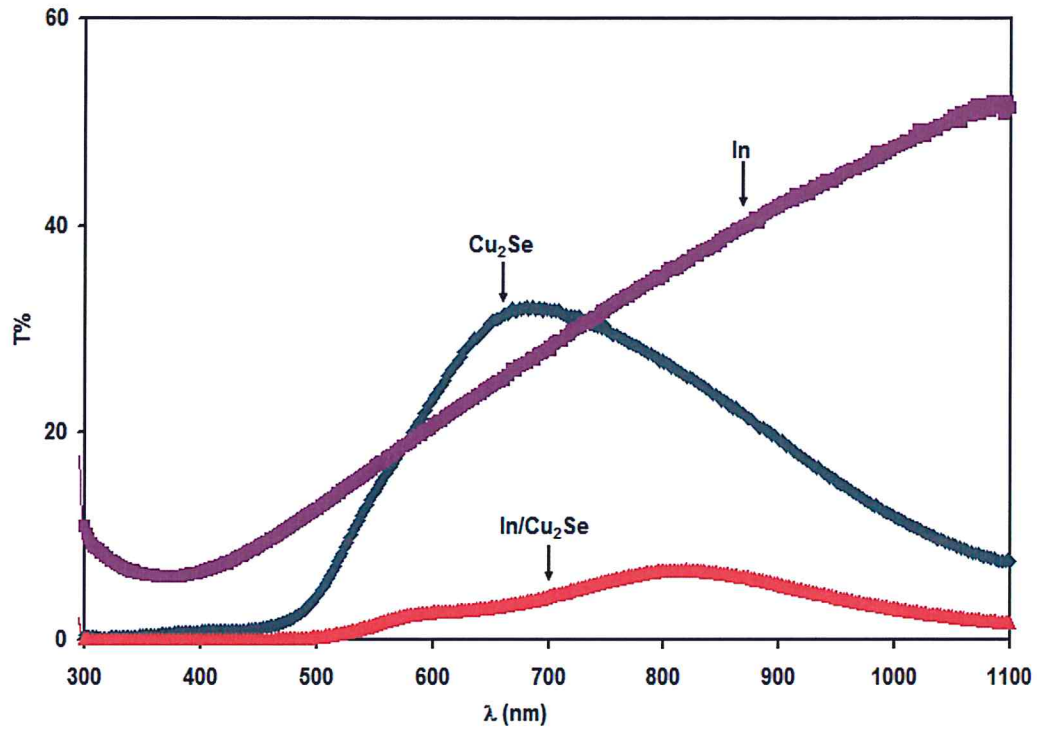


Figure 4.2.1 The optical transmittance for Indium, Copper Selenide on glass and Copper Selenide on Indium substrates.

As it is noticeable from figure 4.2.2, which shows the T% for glass/La (150 nm), glass/Cu₂Se and La/Cu₂Se, as the incident light wave length is increased to 336 nm, the T% for La decrease to 56.5% after that it increases to a constant value of nearly 92.8%. Despite La has relatively high transmittance, it has no noticeable effect on the T% for Cu₂Se rather than a decrease to maximum transmittance value of 27.5%.

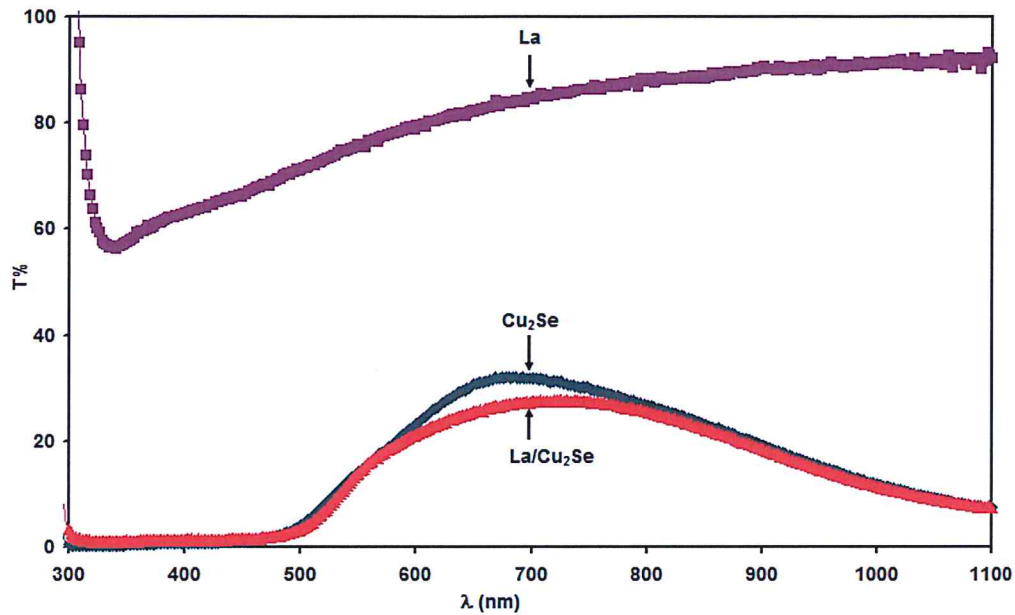


Figure 4.2.2 The optical transmittance for Lanthanum, Copper Selenide on glass and Copper Selenide on Lanthanum substrates.

Figure 4.2.3 displays the transmittance for Pb, Cu₂Se and Pb/Cu₂Se. The T% for Pb increases until it reaches a constant value of 75.6%. Pb is highly transmittive and nearly has no remarkable effect on the transmittance for Cu₂Se.

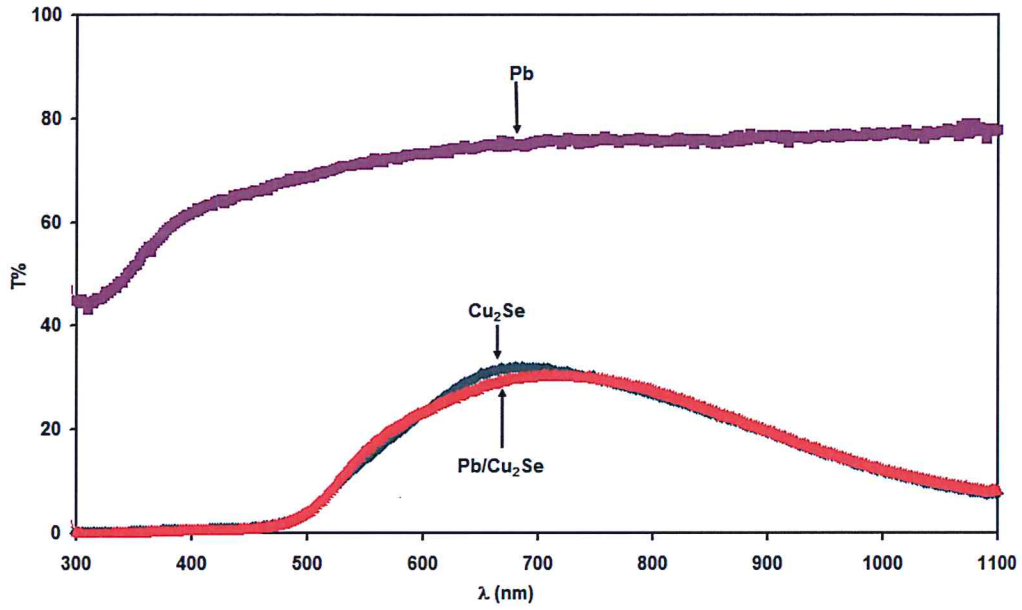


Figure 4.2.3 The optical transmittance for Lead, Copper Selenide on glass and Copper Selenide on Lead substrates.

The R% spectrum for In, Cu₂Se and In/Cu₂Se are shown in figure 4.2.4. As it is observable from the figure, the reflectance for Indium increases with increasing incident light waves length until it reaches a maximum value of 20.5% at 488 nm and then it decreases slowly with increasing λ . Whereas the reflectance for Cu₂Se increases until it reaches maxima of 2.5% at 546 nm. After that, it decreases to reach minima at 840 nm. For all λ greater than 840 nm, R% increases. On the other hand, R% spectra for In/Cu₂Se interface increase with increasing λ of the incident light until it reaches a constant R% of 9.8% then it varies randomly showing noising signal. The figure displayed minima at 570 nm, maximum peak centered at 660 nm which is

corresponding to R value of 14.4% and mutual minimum reflectance with Cu_2Se of 0.5% at 840 nm. After 840 nm, the reflectance increases sharply to 16.38%.

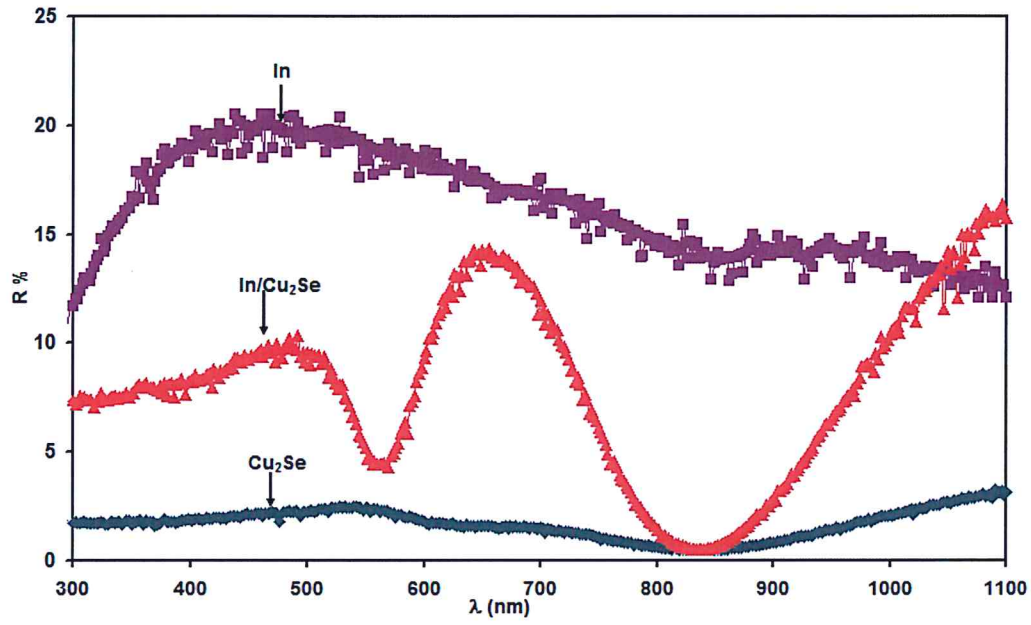


Figure 4.2.4 The optical reflectance for Indium, Copper Selenide on glass and Copper Selenide on Indium substrate.

Figure 4.2.5 illustrates the optical reflectance for glass/La (150 nm), glass/ Cu_2Se and La/ Cu_2Se . As it is shown from the figure, the R% for lanthanum increases until it reaches a constant maximum value of 7% then it decreases as the light wave length is increased up to 808 nm. For λ values larger than 808 nm, reflectance tends to exhibit constant value of $\sim 5\%$. Moreover, the optical reflectance for La/ Cu_2Se increases in the range of 300 to 484 nm up to 6.4%. As the wavelength is increased the reflectance displays two minima, the first one centered at 532 nm and the second one centered at

the minima of Cu_2Se but with 1.3% reflectance. For λ greater than 892 nm, R% exhibit sharp increase until it reaches 11% at 1100 nm.

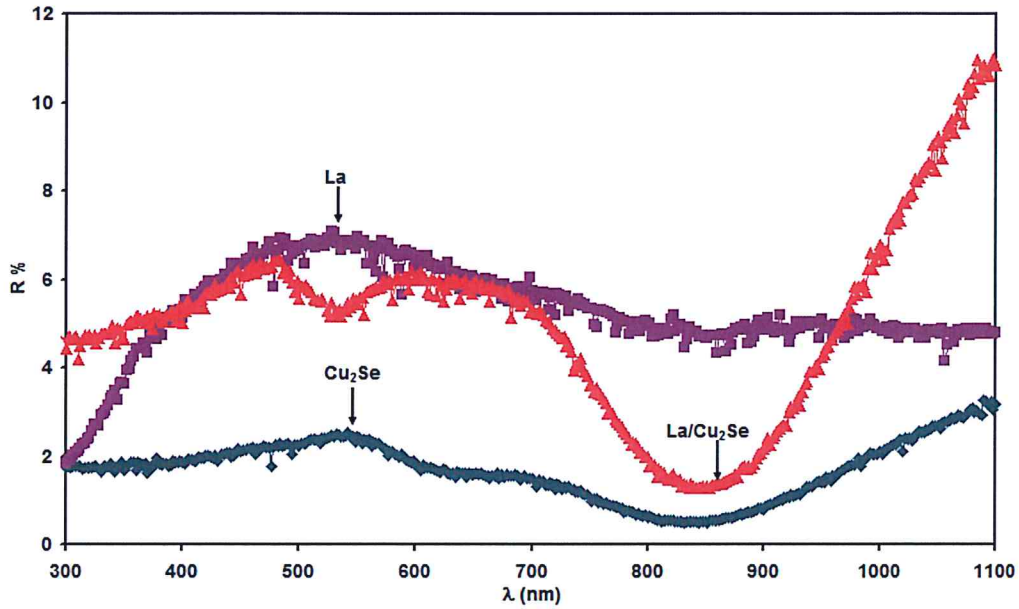


Figure 4.2.5 The optical reflectance for Lanthanum, Copper Selenide on glass and Copper Selenide on Lanthanum substrates.

Figure 4.2.6 shows the reflectance spectrum for Pb, Cu_2Se and Pb/ Cu_2Se . It is readable from the figure that the reflectance for lead metal hardly increases with increasing incident wavelengths up to 362 nm exhibiting a maximum of 8.64%. On the contrary, for higher wavelengths, the R% spectrum decreases to a lower value when λ is increased. The reflectance reaches 4.69% at 1100 nm. Furthermore, the reflectance for Pb/ Cu_2Se increases until $\lambda=488$ nm is reached. It then displays two successive minima which are centered around 536 and 848 nm, respectively. However, in the range of 890 to 1100 nm, the R% is sharply increased up to a maximum value of 14.6%.

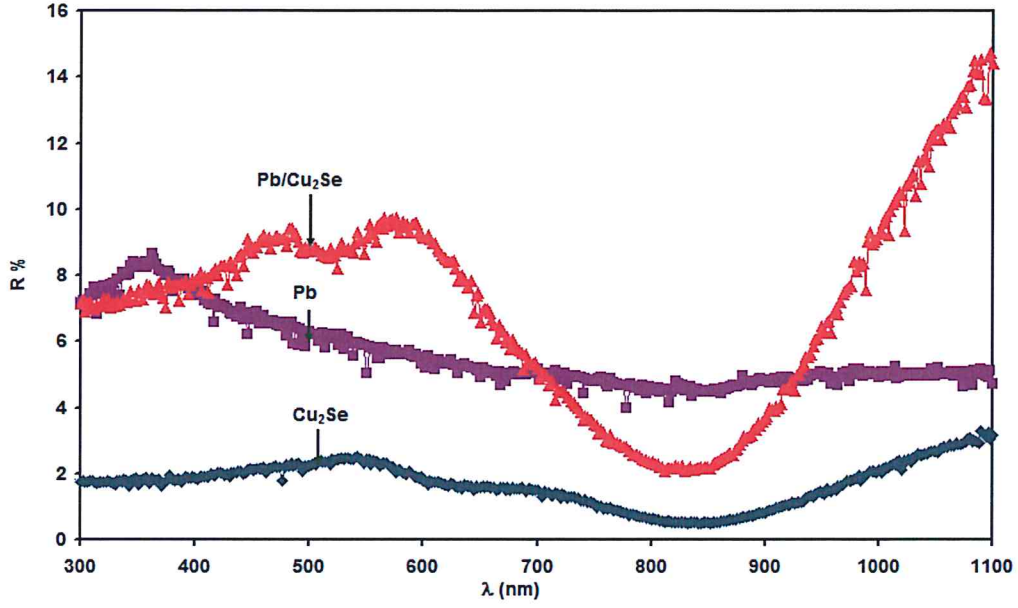


Figure 4.2.6: The optical reflectance for Lead, Copper Selenide on glass and Copper Selenide on Lead substrates

In order to obtain information about the optical properties of the samples, the absorption coefficient (α) was calculated using the relation:

$$T = \frac{(1-R_g)(1-R_m)(1-R_s)e^{-\alpha t}}{1-R_gR_mR_se^{-3\alpha t}} \quad 4.2.1$$

And assuming $R_gR_mR_s \ll 1$ and approaches Zero. Where R_g , R_m and R_s are the reflectance for glass, metal and semiconductor, respectively and t is the thickness. For example, in the case of Cu_2Se and $\text{In}/\text{Cu}_2\text{Se}$, R_m is the reflectance for indium and R_s is the reflectance for Cu_2Se .

The absorption coefficient spectrum for Cu_2Se , which is represented in figure 4.2.7, shows that α increases as the incident light energy is decreased in the range of low

energy regions (1.8- 1.13 eV). In contrast, α decreases sharply with decreasing photon energy in the moderate energy region (2.7-2.3 eV). While it tends to vary slowly about saturation in the high energy region. It is noticeable from figure 4.2.7 that the absorption coefficient for copper selenide on Indium, Lanthanum and Lead have the same behavior of α like that grown on glass, but with different ranges of the energy. The first two regions vary from (1.6-1.13 eV) and (2.75-2.22 eV) for In, (1.6-1.13 eV) and (2.6-2.59 eV) for La and from (1.71-1.13 eV) and (2.78-2.33 eV) for Pb. Moreover, at any energy value, the absorption coefficient increases in the case of Indium and decreases in the presence of Lanthanum and Lead.

The increase in the value of α in the low energy region is attributed to the free carrier absorption in Cu_2Se near the Infra-Red region. One probable reason for the free carrier is the lattice distortion effect that arises from dislocations and impurities. These distortions change the electric dipole moment [51]. Another reason is the degeneracy that raised from the copper to selenium ratio [52]. The low energy strong absorption regions below 1.8 eV is known as free carrier absorption and is ascribed to the lattice distortion. With long wavelengths value near IR region, the light waves can reach the lattice causing atomic vibrations (phonons) which interact with electrons and sets these charge carriers free. The freedom of electrons from the lattice allows the observed absorption spectra [53].

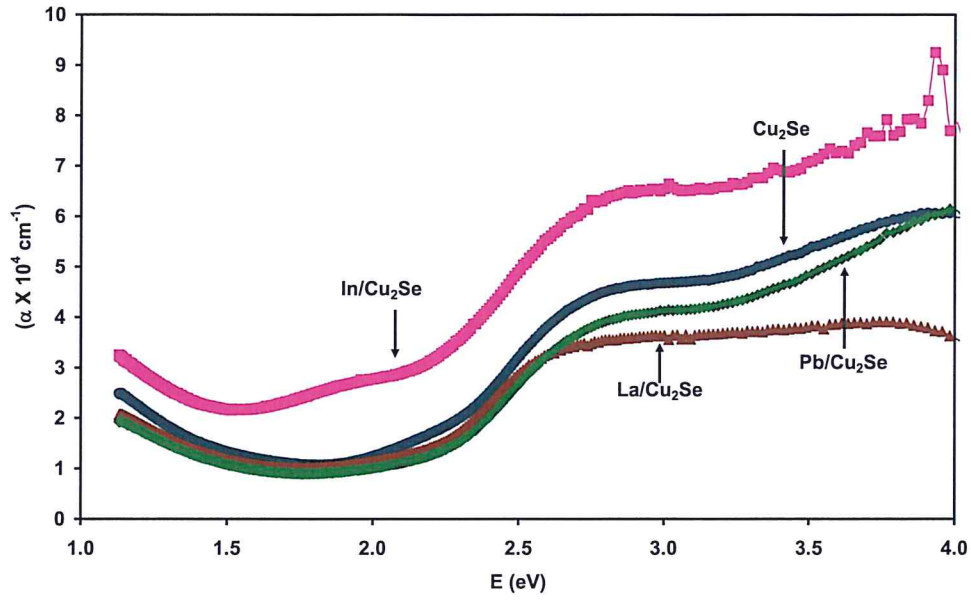


Figure 4.2.7: The optical absorption coefficient for Copper Selenide on glass, Copper Selenide on Indium, Copper Selenide on Lanthanum and copper Selenide on Lead.

The moderate energy region of α spectra where the change is strong is employed to reveal information about the energy band gaps (E_g) of the Cu_2Se and (In, La and Pb)/ Cu_2Se films using Tauc's relation which state that:

$$(\alpha E)^p \propto (E - E_g) \quad 4.2.2$$

Where E is the incident photon energy, E_g is the gap energy and p can take four values: 2, 1/2, 1/3 and 2/3 for direct allowed, indirect allowed, indirect forbidden and direct forbidden band gaps, respectively [54]. In order to determine the type and the value of the band gap, the $(\alpha E)^p$ versus E variations was plotted in figure 4.2.8, 4.2.9 and 4.2.10 for In, La and Pb substrates, respectively. The linearity of the $p=2$ plot is an indication of domination of direct band gaps of all samples.

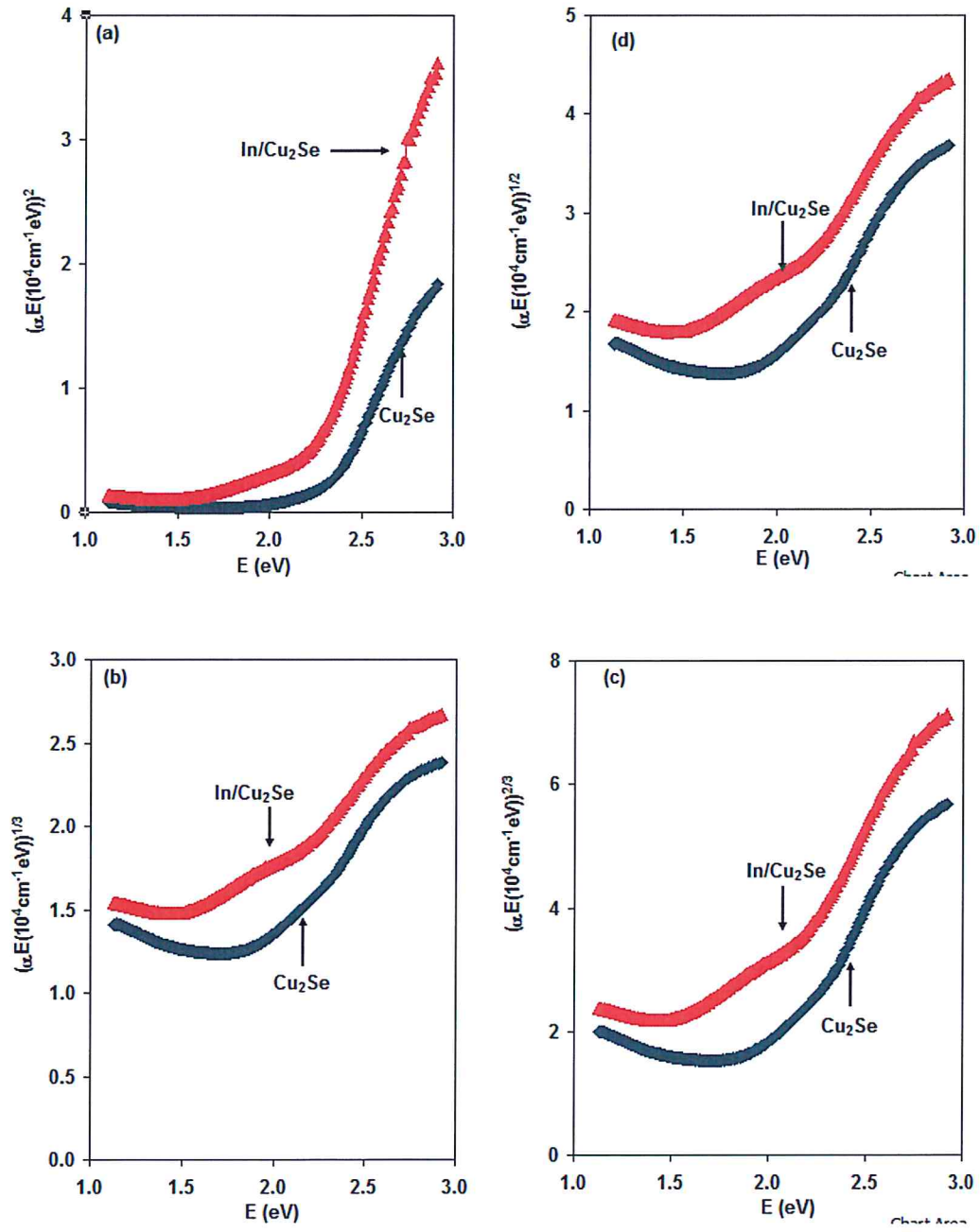


Figure 2.4.8 The $(\alpha E)^{1/p} - E$ variations for glass/ Cu_2Se and $\text{In}/\text{Cu}_2\text{Se}$ for (a) $p=2$, (b) $p=1/3$, (c) $p=3/2$ and (d) $p=1/2$

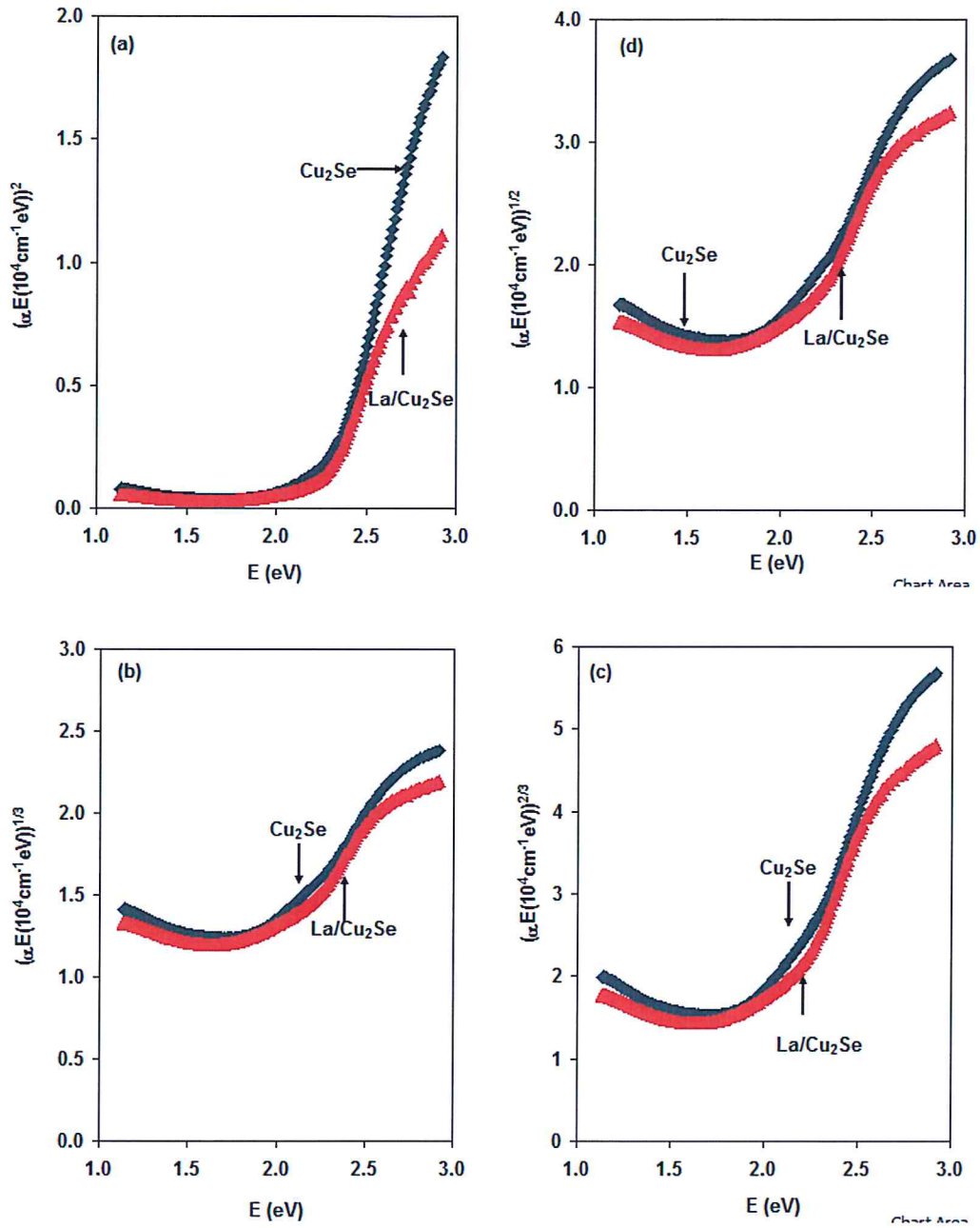


Figure 4.2.9 The $(\alpha E)^{1/p} - E$ variations for glass/Cu₂Se and La/Cu₂Se for (a) $p=2$, (b) $p=1/3$, (c) $p=2/3$ and (d) $p=1/2$

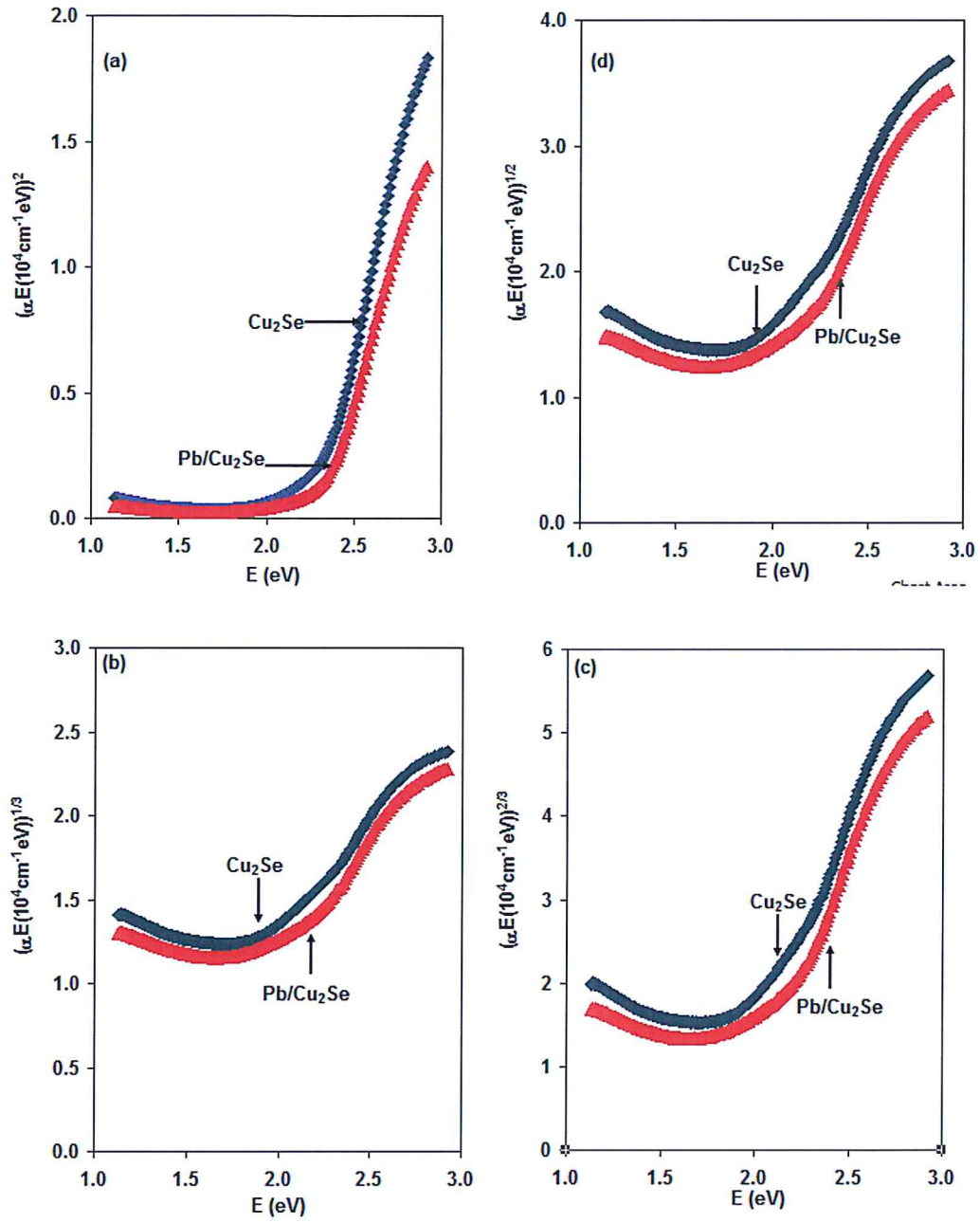


Figure 4.2.10 The $(\alpha E)^{1/p} - E$ variations for glass/ Cu_2Se and $\text{Pb}/\text{Cu}_2\text{Se}$ for (a) $p=2$, (b) $p=1/3$, (c) $p=2/3$ and (d) $p=1/2$

The plot of $(\alpha E)^2$ versus E for Cu_2Se and $\text{In/Cu}_2\text{Se}$, which are illustrated in figure 4.2.11, is fitted to obtain a linear plot where the bang gap is the intercept of the energy axis. The intercept for Cu_2Se curves revealed a band gap of 2.30 eV, this value is in agreement with literature data which state that its gap ranges from 1.9 to 2.3 eV [55]. Moreover, Indium substrate lowered the band gap of Cu_2Se to 2.23 eV.

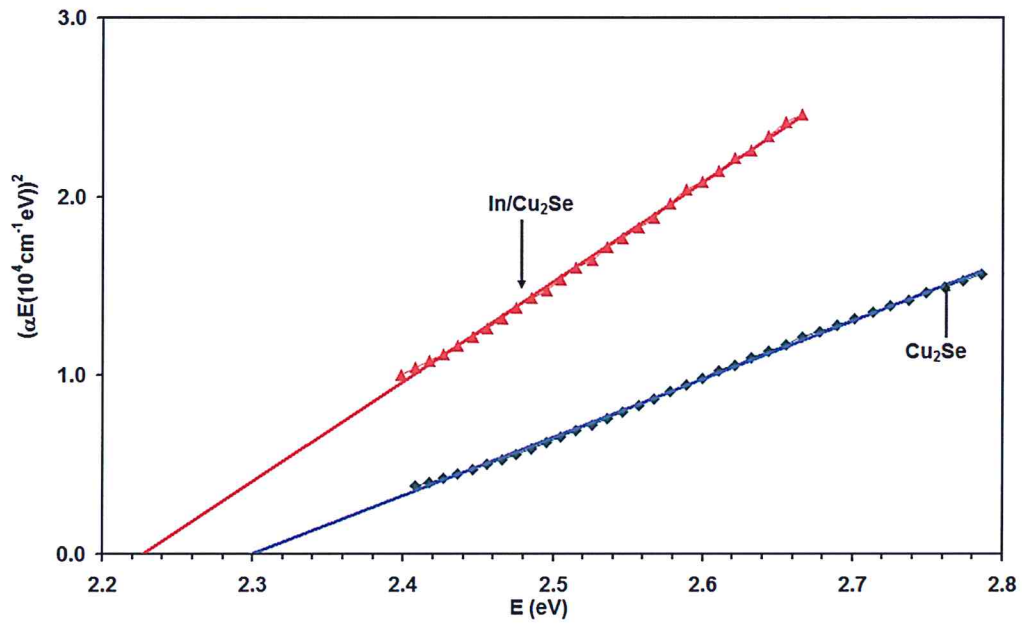


Figure 4.2.11 The $(\alpha E)^2$ versus E plotting for Cu_2Se and $\text{In/Cu}_2\text{Se}$.

In addition, $(\alpha E)^2$ for $\text{La/Cu}_2\text{Se}$ is plotted in figure 4.2.12. As appeared from the plot, $\text{La/Cu}_2\text{Se}$ samples exhibit an energy bang gap lowering. The E_g value in the case of lanthanum is estimated to be 2.24 eV. The same plotting is repeated for $\text{Pb/Cu}_2\text{Se}$ as in figure 4.2.13. Pb substrate reduces the E_g for Cu_2Se to 2.26 eV.

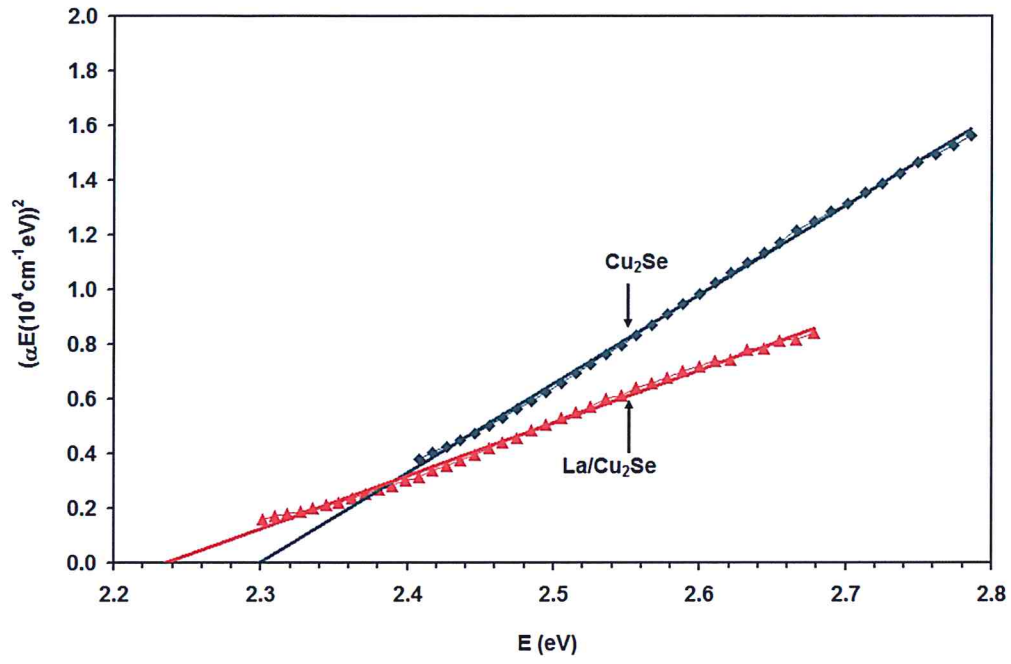


Figure 4.2.12 The $(\alpha E)^2$ versus E plotting for Cu_2Se and $\text{La}/\text{Cu}_2\text{Se}$.

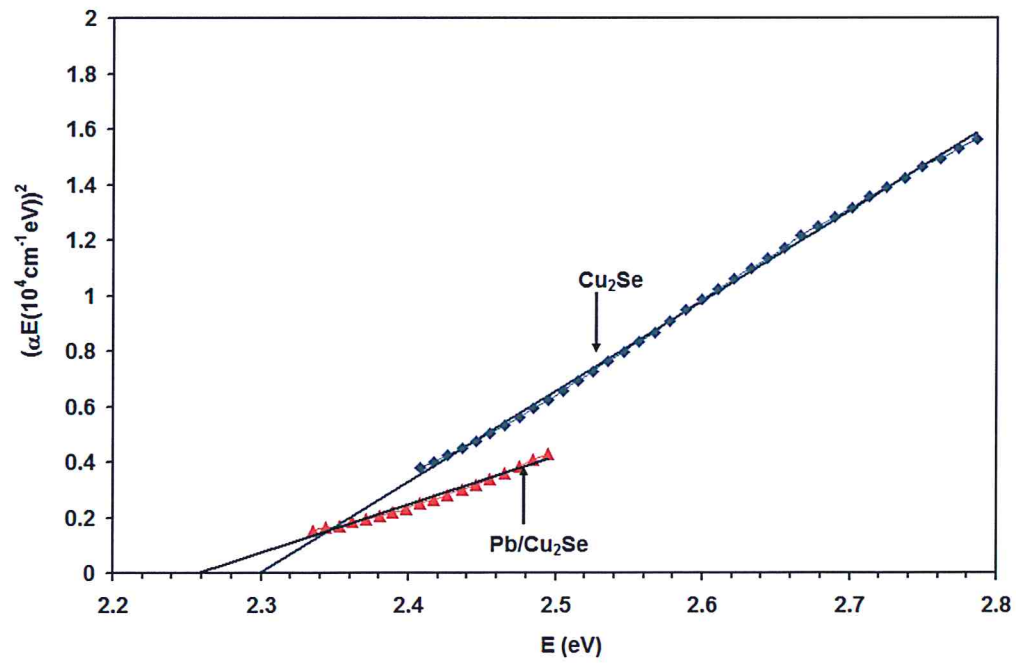


Figure 4.2.13 The $(\alpha E)^2$ versus E plotting for Cu_2Se and $\text{Pb}/\text{Cu}_2\text{Se}$.

From the electronic configuration point of view, the electronic distribution of the Cu and Se atoms reach $3d^{10} 4s^1$ and $4s^2 3d^{10} 4p^4$, respectively. On the other hand, the distribution of In, La and Pb metals reaches $4d^{10} 5s^2 5p^1$, $5s^1 6s^2$ and $4f^{14} 5d^{10} 6s^2 6p^2$, respectively. The metal's higher states make the overlapping of the metals orbitals with that of Cu and Se possible. The upper region of the valence states of Cu_2Se mostly consist of Cu-3d states mixed with the 4p states of Se [56]. X-ray results predicts that the probability of overlapping is high due to the contraction of the lattice parameters that occurred when Cu_2Se is deposited on metals. Furthermore, the decrease in E_g values for In/ Cu_2Se and Pb/ Cu_2Se should have appeared as a result of larger grain sizes as we observed in the XRD analysis.

In addition, recalling that the metals work functions are 3.8, 3.3 and 4.25 eV for In, La and Pb [57-59], respectively, which are smaller than the p-type Cu_2Se work function (6.1 eV [60]), the In, La and Pb/ Cu_2Se form an non-ohmic interface. In this type of interfaces, holes flow from the Fermi level of the Cu_2Se to metal side to reach equilibrium in Fermi levels. As a result of the schottky contact, barrier heights of 0.5, 1.0 and 0.05 eV are formed (electron affinity of Cu_2Se is 3.0 eV [61]). Therefore, the decrease in the energy band gap with metal substrates might be ascribed to the band bending due to energy barrier height formation.

Another reason for the band gap shrinkage in the presence of metallic substrates is the image force lowering. The image charges lowers the potential barrier to the flow of holes leading to the up bending of the valance band [62].

Published works [63] show that the presence of leads as a dopant agent increases the band gap for copper selenide and decreases its absorption coefficient, the amount of change depends on the doping concentration of lead. This behavior is somehow different from our result indicating that the Pb atomic substitution that resulted from the interfacing is not sufficient to make the Pb behave as doping agent.

4.3 Effects of In, La and Pb substrates on the dielectric properties of Cu₂Se

To give further significance for the reflectance and absorption spectra, the effective (ϵ_{eff}), real (ϵ_r) and imaginary (ϵ_{im}) parts of the dielectric constants were calculated.

The following relation is used to determine ϵ_{eff} :

$$R = \frac{(\sqrt{\epsilon_{eff}}-1)^2+k^2}{(\sqrt{\epsilon_{eff}}+1)^2+k^2} \quad 4.3.1$$

In addition, ϵ_r and ϵ_{im} are calculated using:

$$\epsilon_r = \epsilon_{eff} - k^2 \quad \text{and} \quad \epsilon_{im} = 2\sqrt{\epsilon_{eff}}k \quad 4.3.2$$

Where k is the extinction coefficient, $k = a\lambda/4\pi$.

The real part of the dielectric constant for glass/Cu₂Se and In /Cu₂Se are displayed in figure 4.3.1. The dielectric constant decreases as the energy decrease in the IR region until the energy reaches 1.46 eV for both films coated onto glass and Indium substrates. Comparing the In/Cu₂Se spectra with that for glass/Cu₂Se, a significant enhancement in the values of ϵ_r can be observed. The magnitude of the real dielectric constant for the In/Cu₂Se films is much higher than that for glass substrates. Moreover, the spectra for In/Cu₂Se intercept that of glass/Cu₂Se one at an energy value of 1.46 eV. While glass/Cu₂Se spectra show no clear peaks, In/Cu₂Se spectral data shows resonance peaks in the ϵ_r spectra at 2.60, 1.89 eV. Also, an increase in the value of ϵ_r in the high energy (frequency) regions from 1.68 to 3.02 are obtained when Copper selenide was deposited onto Indium instead of glass.

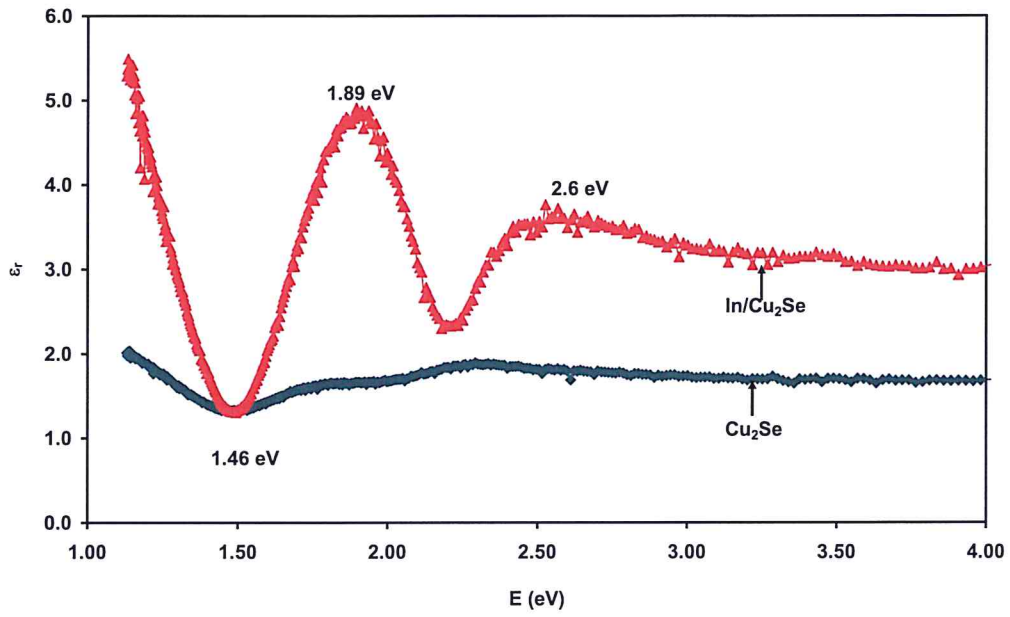


Figure 4.3.1 The real part of the dielectric constant for glass/ Cu₂Se and In/Cu₂Se.

On the other hand, the dielectric spectra for La/Cu₂Se, which are displayed in Fig. 4.3.2, show no clear resonance peaks. Instead, it shows a broaden peak at 2.60 eV. In addition, the behavior of the dielectric constant in the IR region is the same for In/Cu₂Se. However, the presence of Lanthanum remarkably enhanced the value of the dielectric constant such that ϵ_r reaches a value of 2.36 at the high frequency regions.

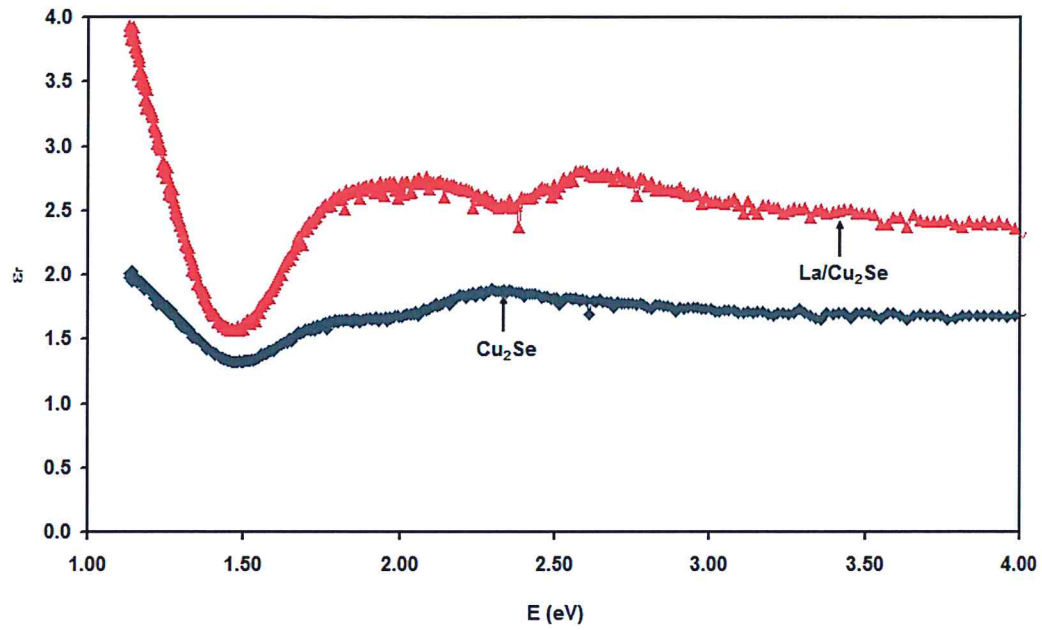


Figure 4.3.2 The real part of the dielectric constant for $\text{Cu}_2\text{Se}/\text{glass}$ and $\text{La}/\text{Cu}_2\text{Se}$.

As appears in Fig. 4.3.3, which shows the real part of the dielectric constant for $\text{Pb}/\text{Cu}_2\text{Se}$, two resonance peaks in ϵ_r spectra of $\text{Pb}/\text{Cu}_2\text{Se}$ appeared at 2.6 and 2.16 eV. Again the behavior of ϵ_r in the IR results in a turning energy point of 1.46 eV. Pb substrate causes an increase in the ϵ_r values. The value of high frequency dielectric constants is 2.93 for $\text{Pb}/\text{Cu}_2\text{Se}$ films, which is higher than that for $\text{La}/\text{Cu}_2\text{Se}$.

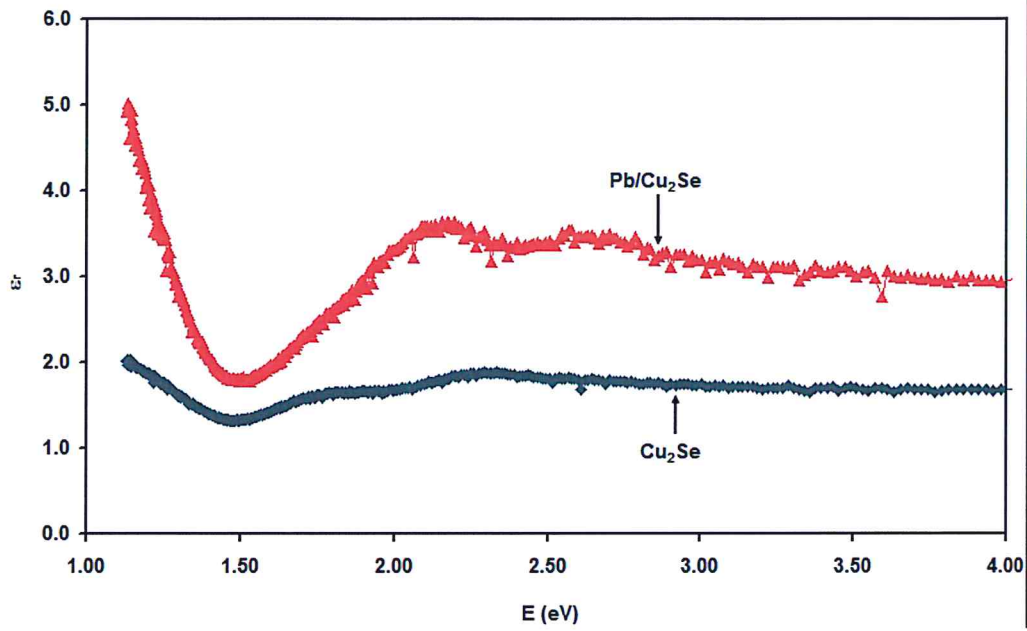


Figure 4.3.3 The real part of the dielectric constant for glass/Cu₂Se and Pb/Cu₂Se.

The 2.6 eV energy values which appeared in presence of In, La and Pb is observed in monoclinic structured Se nanoparticles [64]. The value being 1.86 eV observed in In/Cu₂Se as resonance peaks is assigned to the γ -In₂Se₃ optical band gap [65]. In addition, broaden peak observed at 2.16 eV in Pb/Cu₂Se is due to the transition from the valance band to the conduction one of Cu₂Se as we observed during the calculations of the energy band gap of Pb/Cu₂Se. The 1.46 eV minimum energy which appeared in the case of all substrates (In, La and Pb) arises due to nonstoichiometric atomic distribution of Copper Selenide [66].

The imaginary part of the dielectric (ϵ_{im}) spectra for Cu₂Se are shown in figure 4.3.4, the graph shows one peak centered at 2.71 eV. In addition, ϵ_{im} in the high frequencies regions is about 0.39, which is less than the ϵ_r value for Cu₂Se.

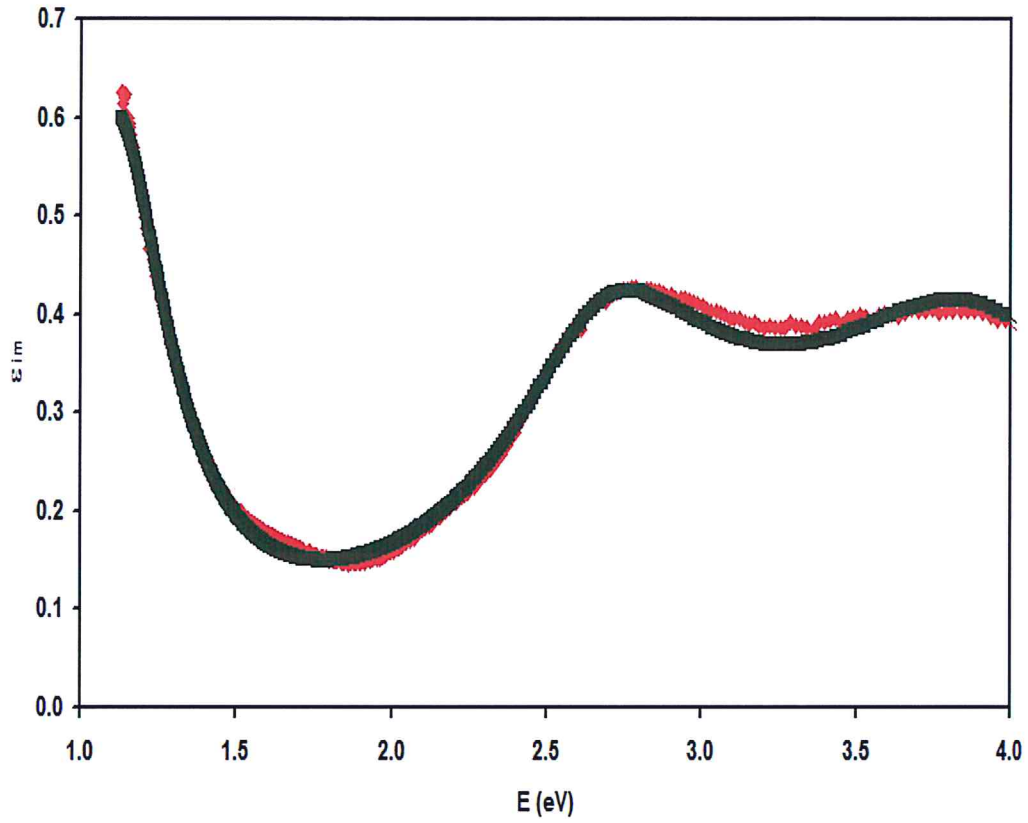


Figure 4.3.4 The imaginary part of the dielectric spectrum for Cu_2Se .

In addition, the ϵ_{im} spectra for In/ Cu_2Se which are displayed in figure 4.3.5 show that the presence of Indium substrate leads to two resonance peaks relative to frequencies of 2.74 eV and 1.89 eV. However, the ϵ_{im} at high frequency regions is 0.7 which is greater than that for Cu_2Se on glass substrate.

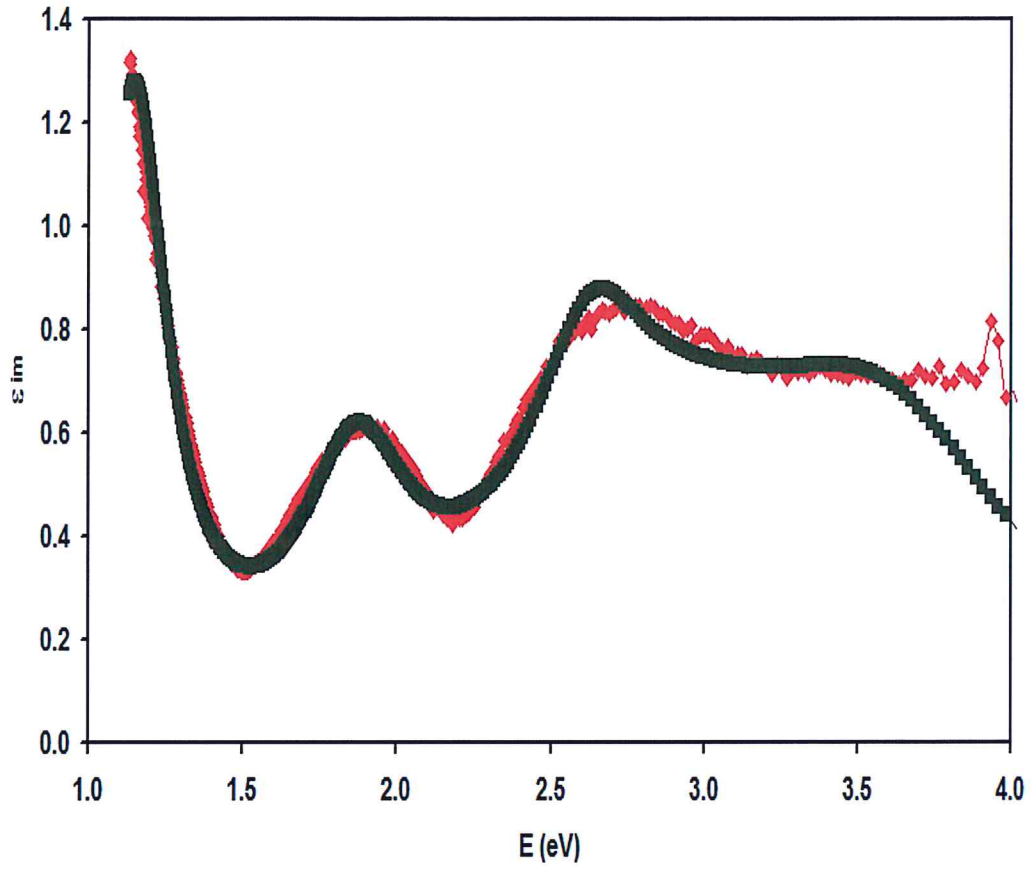


Figure 4.3.5 The imaginary part of the dielectric spectrum for In/Cu₂Se.

As appeared in figure 4.3.6, the ϵ_{im} spectra for La/Cu₂Se decrease until 1.51 eV is reached. After that energy, it remains constants (nearly 0.18) for energies less than 2.20 eV. While it exhibits a resonance peak at 2.62 eV. The ϵ_{im} at high frequencies decreases reaching value of 0.27 at 4.0 eV.

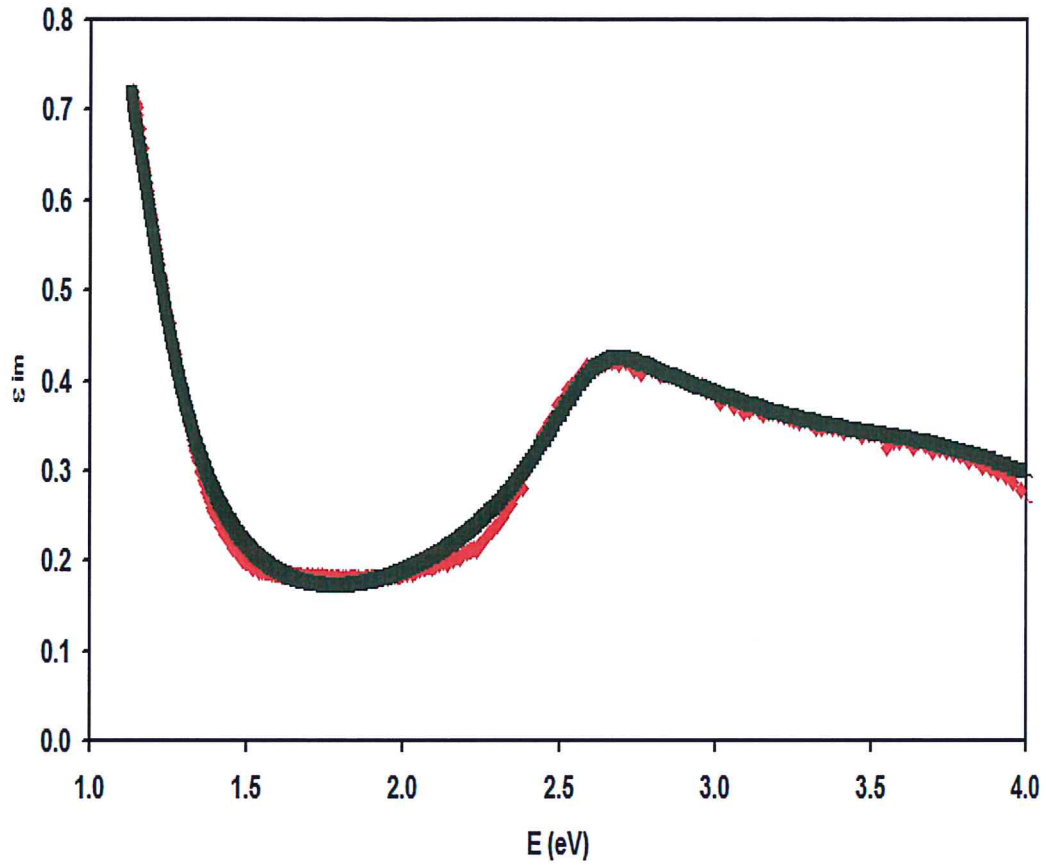


Figure 4.3.6 The imaginary part of the dielectric spectrum for La/Cu₂Se.

The ϵ_{im} spectra for Pb/Cu₂Se are shown in figure 4.3.7. The value of ϵ_{im} decreases until reaches minima of 0.16 at 1.75 eV then increase forming a peak centered at 2.77 eV. In the high frequency regions, the ϵ_{im} value is 0.52 greater than that for glass/Cu₂Se.

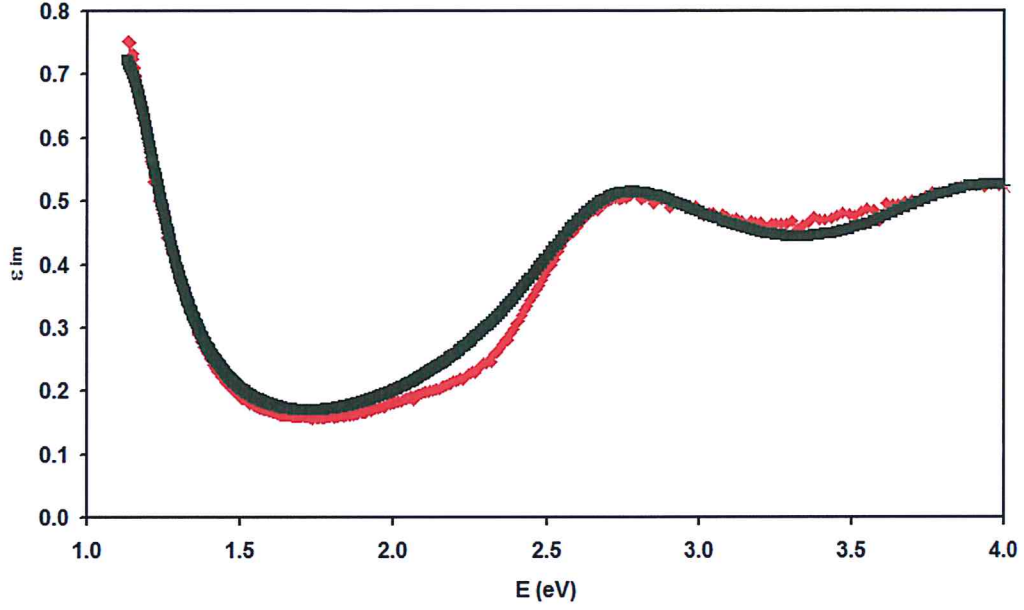


Figure 4.3.7 The imaginary part of the dielectric spectrum for Pb/Cu₂Se.

The variation of ϵ_{im} was modeled in accordance with the Drude-Lorentz Theory in which the imaginary part of the dielectric constant is connected to the incident light frequency through the relation:

$$\epsilon_{im} = \frac{w_{ps}^2 w}{(w_e^2 - w^2)^2 + w^2 \gamma^2} \quad 4.2.6$$

Where γ is the inverse of the electron scattering time (τ_i), w_{ps} is the electron bounded plasma frequency and w_e is the reduced resonance frequency.

The modeling was done by substituting the reduced effective masses (m^*) for Cu₂Se, In/Cu₂Se, La/Cu₂Se and Pb/Cu₂Se. The value of m^* for metal/Cu₂Se was calculated from the following relation:

$$\frac{1}{m^*} = \frac{1}{m^*(metal)} + \frac{1}{m^*(Cu_2Se)} \quad 4.2.7$$

Here $m^* = 0.5 m_0$ [67] and $1.02m_0$ [68] for Copper selenide and Indium respectively. However, m^* for Lanthanum and Lead are assumed to be $1.0m_0$ and $1.5m_0$, respectively.

Five oscillators were used in the modeling. As a result of the modeling, the values of the scattering time (τ), the plasmon frequency (w_p), free charge carrier density (n) and carrier mobility μ are estimated. The obtained values are illustrated in Table 4.2.1. The table suggests that using metal substrates as plasmonic surface, highly improved the material properties. Particularly, the scattering time for the main oscillator ($k=1$) increased from 1.5 fs to 2.5 fs in the presence of In and to 1.55 and to 1.8 fs when the glass substrates were replaced by La and Pb, respectively. The larger the value of τ the less the damping coefficient (γ) value the more mobile the charge carries. As the mobility values which were calculated from the relation $w_p = \sqrt{4\pi ne\mu/\tau}$ show, the drift mobility increases from $5.3 \text{ cm}^2/\text{Vs}$ to $13.0 \text{ cm}^2/\text{Vs}$ and to $8.20 \text{ cm}^2/\text{Vs}$ and to $8.44 \text{ cm}^2/\text{Vs}$ when the glass is replaced by Indium, Lanthanum and Lead substrates, respectively. In addition, the respective free charge carrier density lowers from 8.0×10^{18} to 7.0×10^{18} , to 6.6×10^{18} and to $6.0 \times 10^{18} \text{ cm}^{-3}$. Accordingly, the plasmon frequency in the presence of In and La increase to 2.71 and to 2.64 GHz and remain the same when films are coated onto Pb substrates. The decrease in the free electron density that resulted from the metal/ Cu_2Se interfacing is ascribed to the schottky nature of interfacing. In schottky type interfaces holes flow from semiconductor to metal surface to reach the equilibrium Fermi level. Another reason is the bond formation at the interface between the two materials. The bond formation is usually accompanied with reduction of free charge density owing to charge neutralization.

The obtained values of plasmon frequency being in the range of 2.0-7.04 GHz, nominate the metal/Cu₂Se interfaces for use in communication technology as microwave receivers. The value of the plasmon frequency indicate that all waves whose frequency is less than higher frequencies are allowed to pass. Thus, the samples are promising microwave filters.

Published studies on Au/InSe and Y/InSe show that the conduction is dominated by the resonant plasmon-electron interactions at the metals/InSe interfaces. Also, they are applicable in terahertz technology [69].

Table 4.3.1 Optical conductivity parameters for glass/Cu₂Se, In/Cu₂Se, La/Cu₂Se and Pb/Cu₂Se films.

	Cu ₂ Se					In/Cu ₂ Se					La/Cu ₂ Se					Pb/Cu ₂ Se				
	1	2	3	4	5	1	2	3	4	5	1	2	3	4	5	1	2	3	4	5
τ_i (fs)	1.50	1.00	0.50	0.45	0.30	2.50	1.60	1.50	0.50	0.60	1.55	1.40	0.50	0.30	0.10	1.80	1.00	0.50	0.45	0.30
w_e ($\times 10^{15}$)	1.70	4.10	4.40	6.00	6.30	1.75	2.85	4.00	4.50	5.50	1.62	4.00	4.40	6.00	6.00	1.70	4.10	4.40	6.20	6.30
n ($\times 10^{18}$ cm ⁻³)	8.00	7.00	20.0	53.0	8.00	7.00	6.00	8.00	32.0	37.0	6.60	2.60	14.0	40.0	5.00	6.00	5.00	22.0	53.0	8.00
μ (cm ² /Vs)	5.30	3.50	1.80	1.60	0.40	13.0	8.30	7.80	2.60	0.40	8.20	7.40	2.63	1.60	0.11	8.44	4.70	2.34	2.10	0.30
w_{pi} (GHz)	2.38	2.22	3.76	6.12	2.38	2.71	2.50	2.89	5.78	6.22	2.64	1.66	3.85	6.51	2.30	2.38	2.17	4.55	7.06	2.74

Chapter Five

Conclusions and Further Work

In this thesis, we have investigated the structural, optical and dielectric properties of copper selenide thin films which are grown onto transparent metallic substrates. The metals/semiconductor interfaces which form schottky type of contact between the metals and CuSe have shown that the interfaces exhibit structural modifications based on the metal substrate. Using indium or lead substrates enhances the structural parameters and reduces the defect at the CuSe surfaces. It also improves the atomic ordering as observed from the decrease in the stacking faults percentage. As a result, Indium and Lead substrates increase the grain size to 36 and 33 nm, respectively. On the contrary, lanthanum increased the defect density from 5.02×10^{11} to 16.87×10^{11} line/cm² and lowered the atomic ordering. On the other hand, the optical analysis has shown slight shift in the energy band gap value regardless of the metal type. The energy band gaps are 1.90, 2.23, 2.24 and 2.26 eV for (glass, In, La and Pb)/CuSe. The presence of transparent metal substrates as plasmonic surface improved the optical conductivity parameters. Namely, in the presence of metal substrates, CuSe became more appropriate for optoelectronic device fabrication. Since the charge carriers became more mobile and have larger plasmon frequency values they are attractive for the production of band pass/stop filters. Since the charge carriers mobility increased from 5.30 cm²/Vs to 13.0, 8.20 and 8.44 cm²/Vs for (In, La and Pb)/CuSe and have larger plasmon frequency values of they are attractive for the production of band pass/stop filters.

References

- [1] Z. M Saleh., H. Nasser, E. Özkol, A. Bek, and R. Turan. "Advanced plasmonic interfaces for optimized light trapping in photovoltaics." In *Journal of Physics: Conference Series*, vol. 869, no. 1, p. 012043. IOP Publishing, 2017.
- [2] Zheng, Gaige, Xiujuan Zou, Yunyun Chen, Linhua Xu, and Weifeng Rao. "Fano resonance in graphene-MoS₂ heterostructure-based surface plasmon resonance biosensor and its potential applications." *Optical Materials* 66 (2017): 171-178.
- [3] Cao, En, Weihua Lin, Mengtao Sun, Wenjie Liang, and Yuzhi Song. "Exciton-plasmon coupling interactions: from principle to applications." *Nanophotonics* 7, no. 1 (2018): 145-167.
- [4] Zhang, Tian, Jinzan Zhou, Jian Dai, Yitang Dai, Xu Han, Jianqiang Li, Feifei Yin, Yue Zhou, and Kun Xu. "Plasmon induced absorption in a graphene-based nanoribbon waveguide system and its applications in logic gate and sensor." *Journal of Physics D: Applied Physics* 51, no. 5 (2018): 055103.
- [5] Han, Xu, and Tao Wang. "Tunable plasmon induced transparency in a graphene-based waveguide structure and it's applications in sensing." In *Metamaterials, Metadevices, and Metasystems 2017*, vol. 10343, p. 103432H. International Society for Optics and Photonics, 2017.
- [6] Bai, Jinjun, Yong Li, and Bo Zhao. "Directional light scattering from individual Au nanocup." *Optics Communications* 387 (2017): 208-213.
- [7] A. F. Qasrawi, and Sufyan R. Shehada. "Dielectric dispersion in InSe/CdS bilayers." *Physica E: Low-dimensional Systems and Nanostructures* (2018).
- [8] A. P. Sudha, J. Henry, K. Mohanraj, and G. Sivakumar. "Effect of Na doping on structural, optical, and electrical properties of Cu₂Se thin films prepared by chemical bath deposition method." *Applied Physics A* 124, no. 2 (2018): 164.
- [9] Najla M. Khusayfan, A. F. Qasrawi, and Hazem K. Khanfar. "Impact of Yb, In, Ag and Au thin film substrates on the crystalline nature, Schottky barrier formation and microwave trapping properties of Bi₂O₃ films." *Materials Science in Semiconductor Processing* 64 (2017): 63-70.
- [10] S. E. Al Garni, and A. F. Qasrawi. "Design and characterization of the Ge/Ga₂S₃ heterojunction." *Journal of Electronic Materials* 46, no. 8 (2017): 4848-4856.
- [11] Olfat A.Omareya, A. F. Qasrawi, and S. E. Al Garni. "Effect of Au nanosandwiching on the structural, optical and dielectric properties of the as grown and annealed InSe thin films." *Physica B: Condensed Matter* 520 (2017): 57-64.
- [12] S. R. Alharbi, and A. F. Qasrawi. "Plasmon-electron dynamics at the Au/InSe and Y/InSe interfaces designed as dual gigahertz-terahertz filters." *Optik-International Journal for Light and Electron Optics* 136 (2017): 524-530.
- [13] Najla M. Khusayfan, and Hazem K. Khanfar. "Impact of Mg layer thickness on the performance of the Mg/Bi₂O₃ plasmonic interfaces." *Thin Solid Films* 651 (2018): 71-76.

- [14] C. Guillén, and J. Herrero. "Nanocrystalline copper sulfide and copper selenide thin films with p-type metallic behavior." *Journal of Materials Science* 52, no. 24 (2017): 13886-13896.
- [15] L. N. Maskaveva, E. A. Fedorova, V. F. Markov, M. V. Kuznetsov, O. A. Lipina, and A. V. Pozdin. "Copper (I) Selenide Thin Films: Composition, Morphology, Structure, and Optical Properties." *Semiconductors* 52, no. 10 (2018): 1334-1340.
- [16] Hou, Xin, Pei Xie, Shaolin Xue, Hange Feng, Lingwei Li, Zhiyuan Liu, and Rujia Zou. "The study of morphology-controlled synthesis and the optical properties of CuSe nanoplates based on the hydrothermal method." *Materials Science in Semiconductor Processing* 79 (2018): 92-98.
- [17] Liu, Kegao, Mingxing Jing, Li Zhang, Jing Li, and Lei Shi. "Characterization of the phases and morphology in synthesizing Cu_{2-x}Se and CuSe films." *Integrated Ferroelectrics* 189, no. 1 (2018): 71-77.
- [18] Palve, Balasaheb M., Sandesh R. Jadkar, and Habib M. Pathan. "A simple chemical route to synthesize the umangite phase of copper selenide (Cu₃Se₂) thin film at room temperature." *Journal of Semiconductors* 38, no. 6 (2017): 063003.
- [19] Nelson, P. Issac, R. Arthi, R. Rathes Kannan, T. Ponmudi Selvan, E. Ajitha, A. Ashina, and B. Vidhya. "Influence of heat treatment on the properties of thermally evaporated copper selenide thin films." *Materials Letters* 223 (2018): 14-16.
- [20] Zyoud, Ahed, Khaled Murtada, Hansang Kwon, Hyun-Jong Choi, Tae Woo Kim, Mohammed HS Helal, Maryam Faroun, Heba Bsharat, DaeHoon Park, and Hikmat S. Hilal. "Copper selenide film electrodes prepared by combined electrochemical/chemical bath depositions with high photo-electrochemical conversion efficiency and stability." *Solid State Sciences* 75 (2018): 53-62.
- [21] Palve, Balasaheb M., Vishal S. Kadam, Chaitali V. Jagtap, Sandesh R. Jadkar, and Habib M. Pathan. "A simple chemical route to synthesis the CuSe and CuS counter electrodes for titanium oxide based quantum dot solar cells." *Journal of Materials Science: Materials in Electronics* 28, no. 19 (2017): 14394-14401.
- [22] Gong, Jiangfeng, Yazhou Tian, Ziyuan Yang, Qianjin Wang, Xihao Hong, and Qingping Ding. "High-Performance Flexible All-Solid-State Asymmetric Supercapacitors Based on Vertically Aligned CuSe@Co(OH)₂ Nanosheet Arrays." *The Journal of Physical Chemistry C* 122, no. 4 (2018): 2002-2011.
- [23] A. P. Sudha, J. Henry, K. Mohanraj, and G. Sivakumar. "Effect of Na doping on structural, optical, and electrical properties of Cu₂Se thin films prepared by chemical bath deposition method." *Applied Physics A* 124, no. 2 (2018): 164.
- [24] Nouri, Morteza, H. R. Azimi, Abdolali Moghaddam Saray, and Ramin Yousefi. "S-doping effects on optical properties and highly enhanced photocatalytic performance of Cu₃Se₂ nanoparticles under solar-light irradiation." *Ceramics International* 43, no. 17 (2017): 14983-14988.
- [25] He, Hai-Yan, and Jing Lu. "Chemical Bath Deposition of Undoped and Bi-doped n-Cu₂Se Films and their Optoelectrical Properties." *Nanoscience & Nanotechnology-Asia* 8, no. 2 (2018): 208-215.

- [26] Muthukannan, Abirami, J. Henry, G. Sivakumar, and K. Mohanraj. "Fabrication and characterization of vacuum evaporated Al: CuSe₂ thin films." *Superlattices and Microstructures* 89 (2016): 83-88.
- [27] Kang, Stephen Dongmin, Jan-Hendrik Pöhls, Umut Aydemir, Pengfei Qiu, Constantinos C. Stoumpos, Riley Hanus, Mary Anne White et al. "Enhanced stability and thermoelectric figure-of-merit in copper selenide by lithium doping." *Materials Today Physics* 1 (2017): 7-13.
- [28] Bob B. He. "John Wiley and Sons, Inc". "Two-Dimensional X-Ray Diffraction". 2009.
- [29] Kittel.C. "John Wiley and Sons, Inc". "Introduction to Solid State Physics", 8th edition, (25-32).
- [30] Al Garni, S. E., and A. F. Qasrawi. "Effect of Indium nano-sandwiching on the structural and optical performance of ZnSe films." *Results in physics* 7 (2017): 4168-4173.
- [31] Jian, Sheng-Rui, Jenh-Yih Juang, Chih-Wei Luo, Shin-An Ku, and Kaung-Hsiung Wu. "Nanomechanical properties of GaSe thin films deposited on Si (1 1 1) substrates by pulsed laser deposition." *Journal of Alloys and Compounds* 542 (2012): 124-127.
- [32] Dresselhaus .M. S. "Optical Properties of Solids". "Solid State Physics". (8-11).
- [33] Kuttge, M., H. Kurz, J. Gómez Rivas, J. A. Sánchez-Gil, and P. Haring Bolivar. "Analysis of the propagation of terahertz surface plasmon polaritons on semiconductor groove gratings." *Journal of applied physics* 101, no. 2 (2007): 023707.
- [34] West, Paul R., et al. "Searching for better plasmonic materials." *Laser & Photonics Reviews* 4.6 (2010): 795-808.
- [35] Pannipitiya, Asanka, Ivan D. Rukhlenko, Malin Premaratne, Haroldo T. Hattori, and Govind P. Agrawal. "Improved transmission model for metal-dielectric-metal plasmonic waveguides with stub structure." *Optics Express* 18, no. 6 (2010): 6191-6204.
- [36] Haram, S. K., & Santhanam, K. S. V. (1994). Electroless deposition of orthorhombic copper (I) selenide and its room temperature phase transformation to cubic structure. *Thin Solid Films*, 238(1), 21-26.
- [37] Kaviyarasu, K., Ayeshamariam, A., Manikandan, E., Kennedy, J., Ladchumananandasivam, R., Gomes, U. U., ... & Maaza, M. (2016). Solution processing of CuSe quantum dots: Photocatalytic activity under RhB for UV and visible-light solar irradiation. *Materials Science and Engineering: B*, 210, 1-9.
- [38] Namsani, S., Gahtori, B., Auluck, S., & Singh, J. K. (2017). An interaction potential to study the thermal structure evolution of a thermoelectric material: β -Cu₂Se. *Journal of computational chemistry*, 38(25), 2161-2170.

- [39] Pai, R. R., John, T. T., Lakshmi, M., Vijayakumar, K. P., & Kartha, C. S. (2005). Observation of phase transitions in chemical bath deposited copper selenide thin films through conductivity studies. *Thin Solid Films*, 473(2), 208-212.
- [40] Lybye, D., & Mogensen, M. (2009). Effect of Transition Metal Ions on the Conductivity and Stability of Stabilised Zirconia. *Advances in Solid Oxide Fuel Cells II: Ceramic Engineering and Science Proceedings*, 67-78.
- [41] Watson, E. B., Chmiak, D. J., Hanchar, J. M., Harrison, T. M., & Wark, D. A. (1997). The incorporation of Pb into zircon. *Chemical Geology*, 141(1-2), 19-31.
- [42] Kolesnikov, N. N., Kulakov, M. P., Molchanov, V. N., Schegolev, I. F., Shibaeva, R. P., Simonov, V. I., ... & Vyasilev, O. M. (1995). Comparative study of Tl-2201 single crystals with $T_c = 30$ and 110 K by means of X-ray structural analysis and NMR. *Physica C: Superconductivity*, 242(3-4), 385-392.
- [43] Lee, W., Chen, S. Y., Tseng, E., Gloter, A., & Chen, C. L. (2016). Study of defect structure in ferromagnetic nanocrystalline CeO₂: effect of ionic radius. *The Journal of Physical Chemistry C*, 120(27), 14874-14882.
- [44] Pohl, J., & Albe, K. (2013). Intrinsic point defects in CuInSe₂ and CuGaSe₂ as seen via screened-exchange hybrid density functional theory. *Physical Review B*, 87(24), 245203.
- [45] Singh, K., Patidar, D., & Saxena, N. S. (2005). Composition dependence of effective thermal conductivity and effective thermal diffusivity of Se_{100-x}In_x (x= 0, 5, 10, 15 and 20) chalcogenide glasses. *Journal of Physics and Chemistry of Solids*, 66(6), 946-948.
- [46] Nakhaei, E., Baedi, J., & Disfanee, V. A. (2014). STUDY OF ELECTROCHEMICAL PROPERTIES OF CUGASE 2 CRYSTAL AND THE COMPARISON WITH AUGASE 2 CRYSTAL.
- [47] Wu, Meng, Jun-jie Shi, Min Zhang, Yi-min Ding, Hui Wang, Yu-lang Cen, Wen-hui Guo, Shu-hang Pan, and Yao-hui Zhu. "Modulation of electronic and magnetic properties in InSe nanoribbons: edge effect." *Nanotechnology* 29, no. 20 (2018): 205708.
- [48] Luo, Z. Z., Hao, S., Zhang, X., Hua, X., Cai, S., Tan, G., ... & Dravid, V. P. (2018). Soft phonon modes from off-center Ge atoms lead to ultralow thermal conductivity and superior thermoelectric performance in n-type PbSe-GeSe. *Energy & Environmental Science*, 11(11), 3220-3230.
- [49] Tang, I. N., & Castleman Jr, A. W. (1972). Mass Spectrometric Study of the Gas-Phase Hydration of the Monovalent Lead Ion. *The Journal of Chemical Physics*, 57(9), 3638-3644.
- [50] Monjezi, F., Jamali-Sheini, F., & Yousefi, R. (2018). Pb-doped Cu₃Se₂ nanosheets: Electrochemical synthesis, structural features and optoelectronic properties. *Solar Energy*, 171, 508-518.

- [51] Zhang, Jijun, Linjun Wang, Jiahua Min, Kaifeng Qin, Jian Huang, Ke Tang, Xiaoyan Liang, and Ping Shen. "Annealing of indium-doped CdMnTe single crystals under Cd vapors." *Journal of Crystal Growth* 358 (2012): 12-15.
- [52] Chakrabarti, D. J., and D. E. Laughlin. "The Cu– Se (copper-selenium) system." *Journal of Phase Equilibria* 2, no. 3 (1981): 305-315.
- [53] Khusayfan, Najla M., and Hazem K. Khanfar. "Structural and optical properties of Cu₂Se/Yb/Cu₂Se thin films." *Results in Physics* (2018).
- [54] Fox.M. "Oxford", "Optical Properties of Solids". 2003
- [55] Rong, Fengxia, et al. "Chemical synthesis of Cu₂Se nanoparticles at room temperature." *Materials research bulletin* 47.1 (2012): 92-95.
- [56] Råsaender, Mikael, Lars Bergqvist, and Anna Delin. "Density functional theory study of the electronic structure of fluorite Cu₂Se." *Journal of Physics: Condensed Matter* 25.12 (2013): 125503.
- [57] Williams, R. H., R. R. Varma, and A. McKinley. "Cleaved surfaces of indium phosphide and their interfaces with metal electrodes." *Journal of Physics C: Solid State Physics* 10.22 (1977): 4545.
- [58] Wolff, E. G. "Thermionic emission of boron- and lanthanum- coated boron filaments." *Journal of Applied Physics* 45.9 (1974): 3840-3843.
- [59] Bouley, A. C., T. K. Chu, and G. M. Black. "Epitaxial thin film IV-VI detectors: device performance and basic material properties." *Infrared Detector Materials*. Vol. 285. International Society for Optics and Photonics, 1981.
- [60] Rahmati, Ali, and Asma Farokhipour. "Rectifying Behaviour and Photocatalytic Activity in ZnO Nanorods Array/Ag/CuSe Heterostructure." *Journal of Cluster Science* 30, no. 2 (2019): 521-529.
- [61] Khusayfan, Najla M., and Hazem K. Khanfar. "Structural and optical properties of Cu₂Se/Yb/Cu₂Se thin films." *Results in Physics* (2018).
- [62] Szi.S.M and Kwok.K.Ng, "John Wiley and Sons, Inc", "Physics of Semiconductor Devices". 3rd edition . 2007. (146-150)
- [63] Monjezi, Fatemeh, Farid Jamali-Sheini, and Ramin Yousefi. "Pb-doped Cu₃Se₂ nanosheets: Electrochemical synthesis, structural features and optoelectronic properties." *Solar Energy* 171 (2018): 508-518.
- [64] Rajalakshmi, M., & Arora, A. K. (1999). Optical properties of selenium nanoparticles dispersed in polymer. *Solid state communications*, 110(2), 75-80.
- [65] Li, S., Yan, Y., Zhang, Y., Ou, Y., Ji, Y., Liu, L., ... & Yu, Z. (2014). Monophase γ -In₂Se₃ thin film deposited by magnetron radio-frequency sputtering. *Vacuum*, 99, 228-232.
- [66] Garcia, V. M., Nair, P. K., & Nair, M. T. S. (1999). Copper selenide thin films by chemical bath deposition. *Journal of crystal growth*, 203(1-2), 113-124.

- [67] Alharbi, Seham Reef, and Atef Fayez Qasrawi. "Structural and Optoelectronic Properties of MoO₃/CuSe Interfaces." *physica status solidi (a)* (2019): 1800977.
- [68] Nazzal, Eman O., A. F. Qasrawi, and S. R. Alharbi. "Engineering the Optical and Dielectric Properties of the Ga₂S₃/In/Ga₂S₃ Nanosandwiches via Indium Layer Thickness." *Plasmonics* 13, no. 3 (2018): 1049-1056.
- [69] Alharbi, S. R., and A. F. Qasrawi. "Plasmon-electron dynamics at the Au/InSe and Y/InSe interfaces designed as dual gigahertz-terahertz filters." *Optik* 136 (2017): 524-530.

List of publications

- [1] Fifth palestinian conference on modern trends in mathematics and physics, July 31st – August 2nd, 2016, AAUP, Jenin, Palestine.
- [2] Symposium on Nanotechnology, 27th – 28th June, 2019, Ramallah, Palestine.
- [3] A.N Abu Ghannam, A.F Qassrawi, In situ monitoring of heat assisted oxidation and its effects on the structural, dielectric and optical conductivity parameters of Pb thin films as promising terahertz transmitters, *Plasmonics*, 2019.

الملخص

في هذه الرسالة قمنا بدراسة الخصائص البنائية والضوئية لرقائق سالنيد النحاس المحضرة على قواعد من الزجاج وقواعد شفافة من معادن الانديوم، اللانثانوم والرصاص. لقد تبين أن رقائق سالنيد النحاس المحضرة على قواعد معدنية باستخدام آلية التبخير الفيزيائي الحراري تحت ضغط فراغي مقداره 10^{-5} ملي بار تمتلك خصائص مختلفة معتمدة على نوع المعدن المستخدم. وبالتحديد، بينما حافظت قواعد الانديوم والرصاص على نفس أبعاد الذرات في البلورات المكعبة من سالنيد النحاس، أدى استخدام اللانثانوم إلى قُصر هذه المسافات. بالإضافة إلى ذلك، تبين من التحليلات البنائية أن العوامل البنائية أيضا تتأثر بنوع القاعدة فعلى سبيل التحديد، إن كثافة العيوب ونسبة الأخطاء في التلاصق البلوري والضغط ازدادت عند استخدام اللانثانوم مقارنة بالانديوم أو الرصاص. حجم الحبيبات البلورية تناقص من 28 نانومتر في حالة الزجاج/سالنيد النحاس إلى 16 نانومتر في حالة اللانثانوم/سالنيد النحاس بينما ازداد إلى 36 و 33 نانومتر في وجود قواعد الانديوم والرصاص.

ومن ناحية أخرى بينت دراسات الطيف الضوئي في المدى (300-1100) (نانومتر) أن تأثير القواعد المعدنية على فراغات الطاقة هو ضئيل بينما كان هنالك تأثيرا واضحا على طيف ثابت العازلية. بالإضافة إلى ذلك تبين من تحليلات درود-لورنتس للجزء التخلي من طيف العازلية بأن زمن التشتت في مدى الفمتوثانية ازداد من 1.50 إلى 2.50، 1.55 و 1.80 بوجود قواعد الزجاج و الانديوم واللانثانوم والرصاص. وهذا يعني أن الاحتكاك الالكتروني الذي يؤدي إلى ضعف فعالية الاكترونات الحرة قد قل مما يجعل التوصيل الالكتروني أكثر فعالية. وبالتطابق مع هذه النتيجة تبين أن سرعة الانحراف لكل وحدة مجال كهربائي قد ازدادت في وجود القواعد المعدنية. وتبين أيضا أن قيم التردد البلازموني هي 3.38، 2.71، 1.66 و 2.38 والتي تقع في مدى الجيجاهيرتز. مما يجعل قواعد الانديوم، الرصاص واللانثانوم المتحدة مع سالنيد النحاس قواعد واعدة لإنتاج مرشحات الميكرويف المستخدمة في تكنولوجيا الاتصالات.